On characterizing the viscoelastic electromechanical responses of functionally graded graphene-reinforced piezoelectric laminated composites: Temporal programming based on a semi-a...

Article *in* Mechanics Based Design of Structures and Machines · August 2023

CITATIONS
0

READS
264

4 authors:

Soumyadeep Mondal
National Institute of Technology, Durgapur
13 PUBLICATIONS **34** CITATIONS
SEE PROFILE

Kishor Shingare
Indian Institute of Technology Bombay
23 PUBLICATIONS **173** CITATIONS
SEE PROFILE

Tanmoy Mukhopadhyay
University of Southampton
217 PUBLICATIONS **4,202** CITATIONS
SEE PROFILE

Susmita Naskar
University of Southampton
70 PUBLICATIONS **828** CITATIONS
SEE PROFILE

On characterizing the viscoelastic electromechanical responses of functionally graded graphene-reinforced piezoelectric laminated composites: Temporal programming based on a semi-analytical higher-order framework

S. Mondal[1], K. B. Shingare[1], T. Mukhopadhyay[1], S. Naskar[1,*]

[1]*Faculty of Engineering and Physical Sciences, University of Southampton, Southampton, UK*

[*]*Email Address: S.Naskar@soton.ac.uk (S. Naskar)*

Abstract

The electromechanical responses of single and multi-layered piezoelectric functionally graded graphene-reinforced composite (FG-GRC) plates are studied based on an accurate higher-order shear deformation theory (HSDT) involving quasi-3D sinusoidal plate theory and linear piezoelectricity. These FG-GRC plates are composed of randomly oriented graphene nanoplatelets (GPLs) reinforcing fillers and the piezoelectric PVDF matrix considering two different distribution patterns such as linear- and uniform- distribution (LD and UD) of GPLs across the thickness. The modified Halpin-Tsai (HT) and Rule of mixture (ROM) models are utilized to determine the effective material properties of FG-GRCs. The analytical model of FG-GRCs is extended further to analyze the time-dependent linear viscoelastic electromechanical behaviour of the system based on Biot model of viscoelasticity in the framework of inverse Fourier algorithm. The viscoelastic electromechanical responses include the static deformation and electric responses of simply supported FG-GRC plates which are investigated by considering transverse mechanical and external electrical loading, as well as other critical parameters like aspect ratio and weight fraction of GPLs. The numerical results reveal that the electromechanical response of FG-GRC plates can be enriched due to the addition of a small weight fraction of GPLs. The coupled multiphysics-based computational framework proposed here for predicting the viscoelastic electromechanical behaviour of laminated composites can be exploited for stimulating and developing a wide range of micro-electro-mechanical systems (MEMS) and devices incorporating time-dependent programming features.

Keywords

Active composite laminates; Graphene-reinforced piezoelectric laminates; Functionally graded materials; Piezoelectric effect; Viscoelastic electromechanical responses

1. Introduction

Owing to stimulating multi-functional properties, two-dimensional (2D) materials and their derivatives have emerged to be significantly vital nanomaterials (Saumya et al., 2023). The quest for exploiting extraordinary mechanical properties of 2D graphene (modulus of elasticity, ~1 TPa and strength, 130 GPa) and

high specific surface area (2630 m^2/g) led to the opening of an evolving area of research for developing graphene-based nanocomposites. It can be utilized as an ideal reinforcement candidate for tailoring multifunctional hybrid composites, leading to multifarious applications. The mechanical and interfacial properties of graphene-based composites are significantly enhanced due to the addition of controlled loading contents of graphene. Extensive research is carried out for the prediction of electromechanical behaviour including static and dynamic analysis of graphene-reinforced composite (GRCs) structures such as beam, plate, rod and shell by introducing piezoelectric nanoscale graphene fiber in a non-piezoelectric polyimide matrix (Mukhopadhyay et al., 2021) (Naskar et al., 2022) (Shingare and Naskar, 2023). Graphene is considered as a nanoscale fiber, wherein the effect of size-dependent properties is investigated such as strain and electric field gradient as well as piezoelectric, flexoelectric and surface effects on these GRC structures. The effective piezo elastic and relative permittivity properties of GRC are also probed by using analytical and finite element (FE) micromechanical models. They show a significant enhancement in mechanical and electrical behaviour of GRC structures as it incorporates flexoelectric and surface effects in comparison to the piezoelectric effect. Despite its importance in material design and engineering, research on the behaviors of graphene-reinforced composite is still inadequate.

In the last few years, a new class of materials has emerged as an excellent choice of researchers due to its unique tailorable variation in material properties mainly across the thickness, known as functionally graded materials (FGMs) (Singh et al. 2023a). FGMs show great potential to be used in several areas like automotive, aerospace, aviation and many other engineering domains as shown in Fig. 1. The quest for high performance and exceptional properties including high stiffness, light in weight, durability, and high load-bearing/resistance capacity are the main causes for adopting FGMs (Karsh et al., 2019, 2018; Trinh et al., 2020). The influences of the graded components on the deformation and strength of thick-walled FGM tubes when subjected to internal pressure were examined by Fukui and Yamanaka (1992). Further, Fukui et al. (1993) extended their earlier research by considering these FGM tubes when subjected to uniform thermal loading and examined the effects of gradation of components on residual stresses. By curtailing the circumferential compressive stress at the inner surface of FGM tube, they also proposed an optimal composition. To examine stress intensity factors and transient thermal stresses of FGMs considering cracks, Fuchiyama et al., (1993) utilized an eight-noded quad-axisymmetric element. In order to get more accurate results, they emphasized that the temperature-dependent properties must be accounted for in the investigation. Utilizing optimization and sensitivity techniques, Tanaka et al. (1993) considered FGM property profiles based on the lessening of thermal stresses. Mondal et al. (2022) formulated the closed-form solutions of three-dimensional crack-tip stress fields for a FGM medium under thermo-mechanical loading and investigated the scope of delaying its failure mechanisms. Lu et al. (2006) used stroh-like formalism to analyze a simply supported laminate of functionally graded piezoelectric material (FGPM). Behjat et al. (2011) carried out FE formulation in their paper to investigate

static bending, free vibration and dynamic behaviour of FGPM plates where material properties are graded along thickness direction based on power law. Das and Sarangi (2016) modeled and performed the analysis of an FG beam within ANSYS environment using Solid 186 element. Based on the Navier solution and first-order shear deformation theory (FSDT), Song et al. (2017a) reported the free and forced vibration analyses of FG graphene platelet-reinforced composite (FG GPLRC) laminates. Afterward, by utilizing the same theories, Song et al. (2017b) investigated the buckling and post-buckling behavior of bi-axially compressed FG GPLRC plates. Shen et al. (2017) derived an analytical solution for buckling and post-buckling analyses of FG GPLRC plates rested on elastic foundation. In addition to this, the results of thermal buckling and the post-buckling of GPLRC plates were analyzed by Wu et al. (2017) using the differential quadrature-based iteration method. They showed the increment and decrement of thermal buckling and post-buckling resistance considering different parameters such as weight fraction of GPLs along with their distribution, width-to-thickness, and aspect ratios. Gholami and Ansari (2017) investigated the large deflection and geometrically nonlinear analysis of FG GPLRC plates using analytical solutions. Based on the Navier solution and FSDT, Song et al. (2018) introduced the static and compressive buckling analyses of the FG GPLRC plate. They also reported that the shear correction factor is essential to confirm the accuracy of the mathematical framework that they presented. Using the element-free IMLS-Ritz method and FSDT, Guo et al. (2018) studied the vibration of GPLs reinforced layered composite quadrilateral plates. Gholami and Ansari (2018) used higher-order SDT to find out nonlinear harmonically excited vibration of rectangular FG GPLRC plates based on the variational differential quadrature (DQ). Using the transformed DQ method, Malekzadeh et al. (2018) investigated the vibration of FG GPLRC eccentric annular plates integrated with layers of piezoelectric material. Some of the research investigations in this field combine FGMs and composite structures for achieving a wide range of performances (Barati and Zenkour, 2019; Natarajan et al., 2014) (Assadi and Farshi, 2011). A major interest of current research activities involves the presence of homogeneous strain and electric field in FGM plates concerning the piezoelectric effect, which we discuss in the following paragraph.

In the search for emerging lightweight multi-functional structures, it was revealed that if piezoelectric materials are utilized as distributed sensors/actuators which can be attached to or incorporated into the structure then it accomplishes self-monitoring and self-controlling competencies (Smith and Auld, 1991). These structures are usually named as “smart structures”. Piezoelectric materials generate the electric response to an applied mechanical load by virtue of the direct piezoelectric effect while it deforms due to the electric load by virtue of the inverse effect (Kuai et al., 2013; Maranganti et al., 2006; Tita et al., 2015). For developing high-performing structures, the use of piezoelectric materials as distributed actuators and sensors is related to these direct and inverse effects, respectively. In recent advances, the FG structures integrated with piezoelectric actuators and sensors have received much interest from the application as well as the fundamental research point of view to develop MEMS and technology-based energy harvesters

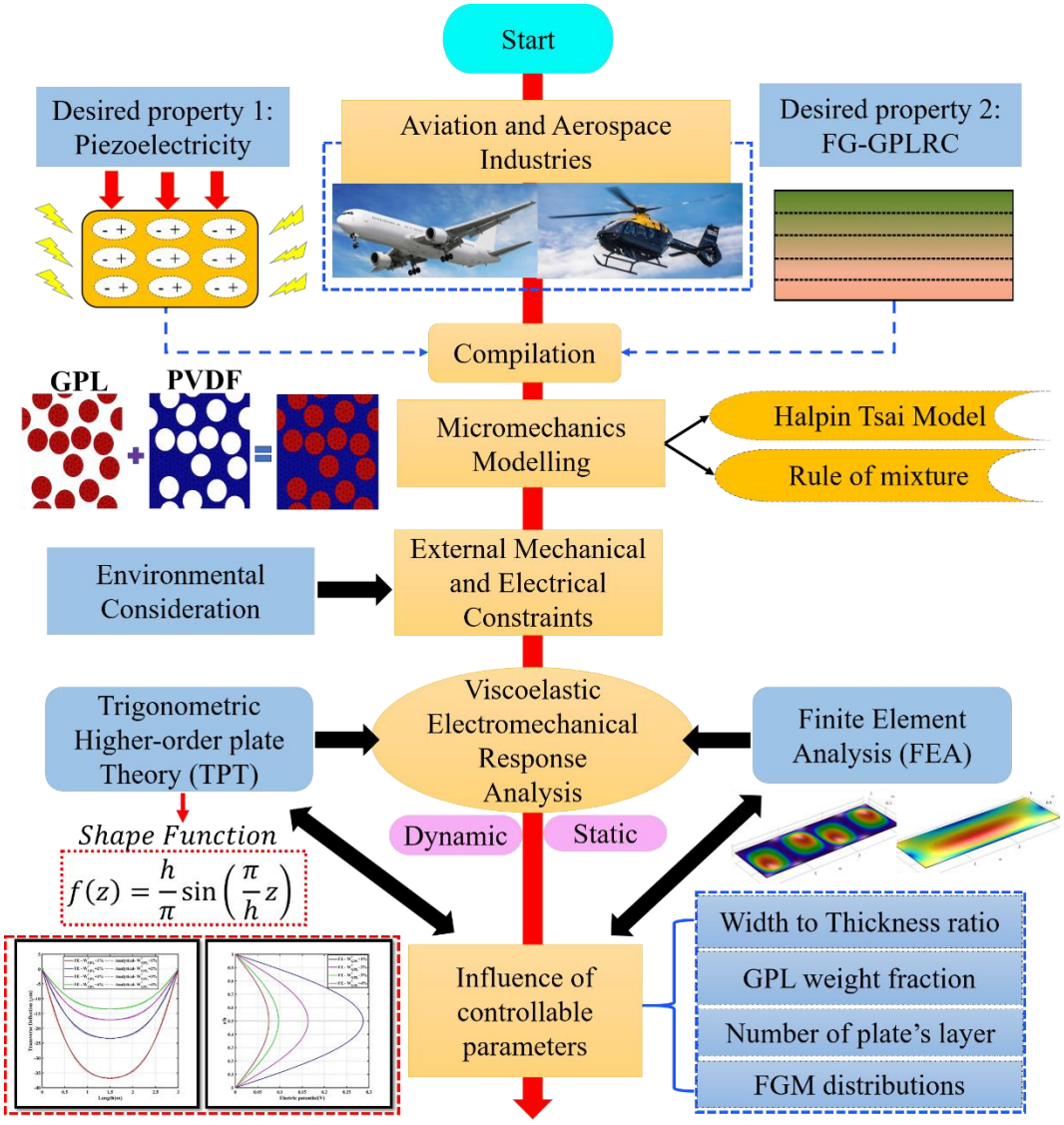

Fig 1. A bird's eye view concerning detailed flowchart of viscoelastic electromechanical analysis of piezoelectric FG-GRC plates for application in various technologically demanding industries.

(Beeby et al., 2006; Yan and Jiang, 2017, 2011). For a better understanding of piezoelectricity phenomena, the concept of piezoelectric effect is described using mathematical relation: $D_i \sim e_{ijk}\varepsilon_{jk}$. In this, D_i, ε_{jk} and e_{ijk} represent the electric displacement vector, the strain tensor and the piezoelectric tensor, respectively. Such piezoelectricity phenomena are found to be present in materials where the inversion symmetry plays a vital role, meaning the material should be non-centrosymmetric.

Consideration of viscoelasticity in smart piezoelectric composite materials makes it more realistic in terms of accurate electromechanical response prediction due to the fact that many of the polymers used in composite structures are inherently viscoelastic in nature. Time and frequency domain analyses of the viscoelastic effect have been reported in composite structures. Aboudi and Cederbaum, 1989 presented a micromechanical analysis of unidirectional fibre composites considering the phases to be viscoelastic in nature.

Salehi and Aghaei, 2005 analyzed axisymmetric viscoelastic circular plates using a non-linear and non-axisymmetric formulation. Wenzel et al., 2009 developed a model to analyze the deflection of viscoelastic (polymeric) cantilevered beams under uniform (adsorption-induced) surface stress. García-Barruetabeña et al., 2013 discussed the interconversion scheme of viscoelastic relaxation modulus from the time-domain and frequency domain and vice-versa. Amoushahi and Azhari, 2014 studied a moderately thick viscoelastic plate using linear finite strip formulations. Mukhopadhyay et al., 2019 incorporated the effect of viscoelasticity into an irregular hexagonal honeycomb lattice following a bottom-up analytical framework in the frequency domain. Jafari and Azhari, 2021 discussed the bending of thick viscoelastic Mindlin plates with different geometries in the time-domain. Singh et al., 2023 showed the usage of extended Kantorovich method (EKM) to analyze IPFG viscoelastic plates embedded with piezo sensory layer.

The review of literature presented on composite/FGM with consideration of graphene platelets clearly specifies that graphene/its derivatives are one of the most promising nanofiller for multiphysical applications. However, until now, to the best knowledge of the authors, there are no (or very few) studies investigating the electric and mechanical response of functionally graded graphene-reinforced piezoelectric composite (FG-GRC) plates with and without consideration of the viscoelastic effect. Such an investigation could offer many exploitable prospects for developing next-generation MEMS and smart structures (note: hereinafter the "FGM" is used for functionally graded material without piezoelectric effect, while "FGPM" is used for functionally graded piezoelectric material). In this article, the electromechanical responses of single and multi-layered piezoelectric functionally graded graphene-reinforced composite (FG-GRC) plates would be studied based on an accurate higher-order shear deformation theory (HSDT) involving quasi-3D sinusoidal plate theory, linear piezoelectricity and the effect of viscoelasticity. The results would be further validated with separate finite element (FE) modeling extensively. The reason for taking HSDT as a benchmark over classical plate theories (CPT) is due to its ability to incorporate thickness deformation ($\varepsilon_z \neq 0$) and transverse shear deformation.

The contribution of this work is aimed at predicting the viscoelastic electromechanical performance of simply supported FG-GRC plates with and without consideration of piezoelectric effect using analytical and FE approach under generic loading conditions (quasi 3D sinusoidal distributed load). In the process, we would investigate different critical parameters such as weight fraction of GPLs and aspect ratios concerning direct and inverse piezoelectric effects. An overview of the comprehensive analysis concerning the current research work is systematically presented in Fig. 1. This article is structured as: **Section 2:** the basic mathematical formulations based on quasi-3D sinusoidal plate theory and linear viscoelasticity are introduced; **Section 3:** the details of FE models are presented; **Section 4:** the numerical results are discussed for single and multilayer FG-GRC plates to investigate their electromechanical responses, including the effect of viscoelasticity; Finally, the article is summarized with concluding remarks and critical perspectives in **Section 5**.

2. Theoretical formulation

2.1 Geometric consideration

Figure 2 shows a schematic of single-layered rectangular plates made of functionally graded piezoelectric material (FGPM) with width a, length b and height h and it is associated with Cartesian coordinate system $\left(0 \le x \le b, 0 \le y \le a, -\frac{h}{2} \le z \le \frac{h}{2}\right)$. The FGPM plate is assumed to consist of polyvinylidene fluoride (PVDF) matrix and graphene platelets (GPLs) reinforcement. The top surface of FGPM plate is subjected to a transversely distributed load p_0. This mechanical load is dependent on only two in-plane spatial coordinates x and y while an external electric voltage V is applied in between its top and bottom plate surface. Variation of material properties is considered to be continuous in nature (Nomura and Sheahen, 1997) and it is varied only along its thickness direction i.e., z-axis. The present formulation can also be applicable to multilayer laminates (with number of layers N_L) which is explained later in Section 4.2.

2.2 Kinematic relations

Considering the quasi-3D sinusoidal plate theory (Zenkour, 2007) and the shape function proposed by Levy (1877), Stein (1986) and Touratier (1991), the displacement field (u, v, w) of any point within the volume of interest along three orthonormal directions can be expressed in the following form (Zenkour and Hafed, 2020):

$$u(x,y,z) = u_0(x,y) - z\frac{\partial w_0(x,y)}{\partial x} + \frac{h}{\pi}\sin\left(\frac{\pi}{h}z\right)\psi_x(x,y) \tag{1a}$$

$$v(x,y,z) = v_0(x,y) - z\frac{\partial w_0(x,y)}{\partial y} + \frac{h}{\pi}\sin\left(\frac{\pi}{h}z\right)\psi_y(x,y) \tag{1b}$$

$$w(x,y,z) = w_0(x,y) + \cos\left(\frac{\pi}{h}z\right)\varphi_z(x,y) \tag{1c}$$

where (u_0, v_0) and w_0 indicate the in-plane and out-of-plane displacements of any point respectively on the mid-plane $(z = 0)$ and (ψ_x, ψ_y) indicate the respective rotations of the transverse normal about y and x-axis. $\varphi_z(x,y)$ is for accounting the stretching effect of the plate. Contrary to typical first-order shear deformation theory, the present trigonometric plate theory does not require any shear correction coefficient.

- **Assumptions:**
  1. Any straight lines perpendicular to mid-surface before deformation stay straight after its deformation.
  2. There will be the contribution of bending and shear both in total transverse displacement.

$$w_0(x,y) = w_{0b}(x,y) + w_{0s}(x,y) \tag{2}$$

  3. Rotation function (ψ_x, ψ_y) are approximated as respective slopes of shear transverse deflection:

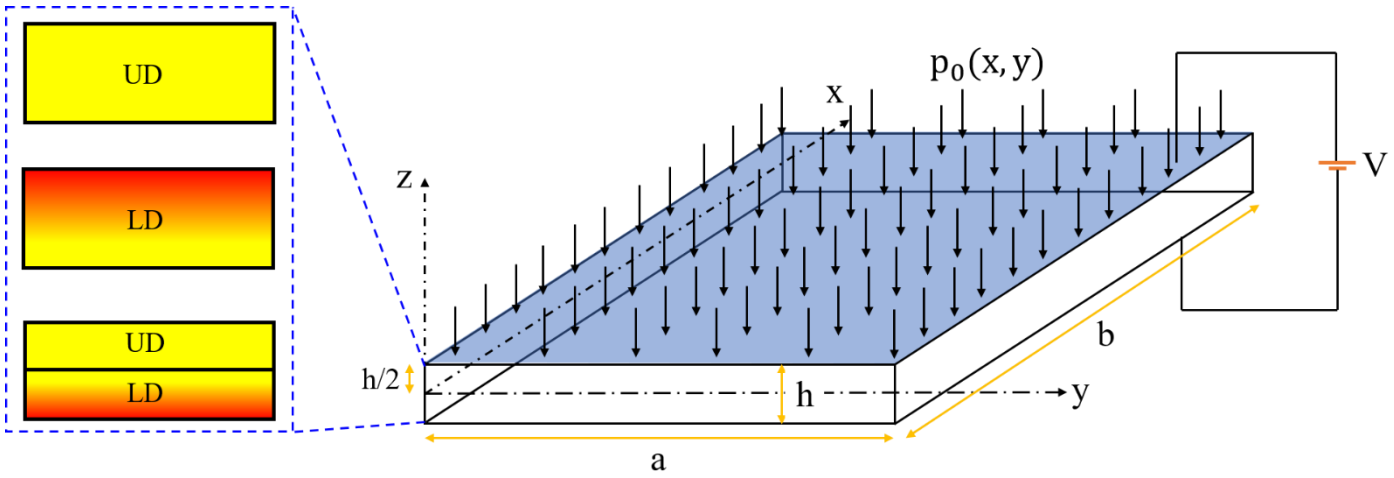

Fig 2. Schematic of FGPM plate subjected to electromechanical loadings and associated cross-sections.

$$\psi_x(x,y) = \frac{\partial w_{0s}}{\partial x} \text{ and } \psi_y(x,y) = \frac{\partial w_{0s}}{\partial y}. \tag{3}$$

Considering these assumptions in Eq. (1), we get the following simpler forms:

$$u(x,y,z) = u_0(x,y) - z\frac{\partial w_{0b}(x,y)}{\partial x} - f_1(z)\frac{\partial w_{0s}(x,y)}{\partial x} \tag{4a}$$

$$v(x,y,z) = v_0(x,y) - z\frac{\partial w_{0b}(x,y)}{\partial y} - f_1(z)\frac{\partial w_{0s}(x,y)}{\partial y} \tag{4b}$$

$$w(x,y,z) = w_{0b}(x,y) + w_{0s}(x,y) + f_2(z)\varphi_z(x,y) \tag{4c}$$

where $f_1(z) = z - \frac{h}{\pi}\sin\left(\frac{\pi}{h}z\right)$ and $f_2(z) = \cos\left(\frac{\pi}{h}z\right)$ are derived from the assumed shape function. Neglecting Von-Karmen non-linear terms in strain formulae, we can derive the following linear strain-displacement relations from Eq. (4):

$$\varepsilon_x = \frac{\partial u}{\partial x} = \frac{\partial u_0}{\partial x} - z\frac{\partial^2 w_{0b}}{\partial x^2} - f_1(z)\frac{\partial^2 w_{0s}}{\partial x^2} = \varepsilon_x^0 + z\kappa_x + f_1(z)\eta_x \tag{5a}$$

$$\varepsilon_y = \frac{\partial v}{\partial y} = \frac{\partial v_0}{\partial y} - z\frac{\partial^2 w_{0b}}{\partial y^2} - f_1(z)\frac{\partial^2 w_{0s}}{\partial y^2} = \varepsilon_y^0 + z\kappa_y + f_1(z)\eta_y \tag{5b}$$

$$\varepsilon_z = \frac{\partial w}{\partial z} = f_2'(z)\varphi_z \tag{5c}$$

$$\gamma_{xy} = 2\varepsilon_{xy} = \frac{\partial u}{\partial y} + \frac{\partial v}{\partial x} = \frac{\partial u_0}{\partial y} + \frac{\partial v_0}{\partial x} - 2z\frac{\partial^2 w_{0b}}{\partial x\,\partial y} - 2f_1(z)\frac{\partial^2 w_{0s}}{\partial x\,\partial y} = \gamma_{xy}^0 + z\kappa_{xy} + f_1(z)\eta_{xy} \tag{5d}$$

$$\gamma_{yz} = 2\varepsilon_{yz} = \frac{\partial v}{\partial z} + \frac{\partial w}{\partial y} = f_2(z)\left(\frac{\partial w_{0s}}{\partial y} + \frac{\partial \varphi_z}{\partial y}\right) = f_2(z)\gamma_{yz}^0 \tag{5e}$$

$$\gamma_{xz} = 2\varepsilon_{xz} = \frac{\partial u}{\partial z} + \frac{\partial w}{\partial x} = f_2(z)\left(\frac{\partial w_{0s}}{\partial x} + \frac{\partial \varphi_z}{\partial x}\right) = f_2(z)\gamma_{xz}^0 \tag{5f}$$

where $\varepsilon_x^0 = \frac{\partial u_0}{\partial x}$, $\varepsilon_y^0 = \frac{\partial v_0}{\partial y}$, $\gamma_{xy}^0 = \frac{\partial u_0}{\partial y} + \frac{\partial v_0}{\partial x}$, $\kappa_x = -\frac{\partial^2 w_{0b}}{\partial x^2}$, $\kappa_y = -\frac{\partial^2 w_{0b}}{\partial y^2}$, $\kappa_{xy} = -2\frac{\partial^2 w_{0b}}{\partial x\,\partial y}$, $\eta_x = -\frac{\partial^2 w_{0s}}{\partial x^2}$, $\eta_y = -\frac{\partial^2 w_{0s}}{\partial y^2}$, $\eta_{xy} = -2\frac{\partial^2 w_{0s}}{\partial x\,\partial y}$, $\gamma_{yz}^0 = \left(\frac{\partial w_{0s}}{\partial y} + \frac{\partial \varphi_z}{\partial y}\right)$ and $\gamma_{xz}^0 = \left(\frac{\partial w_{0s}}{\partial x} + \frac{\partial \varphi_z}{\partial x}\right)$. We can observe here the existence of non-zero transverse strains ($\varepsilon_z \neq 0$) which is also a characteristic of any typical shear deformation plate theories.

Accounting Maxwell's equation, the variation of electric potential ($\bar{\phi}$) through thickness can be approximated by the following equation proposed by Quek and Wang (2000):

$$\bar{\phi} = -\cos\left(\frac{\pi}{h}z\right)\phi(x,y) + \frac{2V}{h}z = -f_2(z)\phi(x,y) + \frac{2V}{h}z \tag{6}$$

where ϕ denotes the distribution of electric potential induced in mid-plane. The electric field components E can be given by:

$$E = \begin{pmatrix} E_x \\ E_y \\ E_z \end{pmatrix} = \begin{pmatrix} -\frac{\partial \bar{\phi}}{\partial x} \\ -\frac{\partial \bar{\phi}}{\partial y} \\ -\frac{\partial \bar{\phi}}{\partial z} \end{pmatrix} = \begin{pmatrix} f_2(z)\frac{\partial \phi}{\partial x} \\ f_2(z)\frac{\partial \phi}{\partial y} \\ f'_2(z)\phi - \frac{2V}{h} \end{pmatrix} \tag{7}$$

2.3 Constitutive equations and function resultants

General constitutive relations for any piezoelectric material can be given by following two equations of actuation- and sensing- law (Li et al., 2020):

$$\begin{pmatrix} \sigma_x \\ \sigma_y \\ \sigma_z \\ \tau_{yz} \\ \tau_{xz} \\ \tau_{xy} \end{pmatrix} = \begin{pmatrix} c_{11}(z) & c_{12}(z) & c_{13}(z) & 0 & 0 & 0 \\ c_{12}(z) & c_{22}(z) & c_{23}(z) & 0 & 0 & 0 \\ c_{13}(z) & c_{23}(z) & c_{33}(z) & 0 & 0 & 0 \\ 0 & 0 & 0 & c_{44}(z) & 0 & 0 \\ 0 & 0 & 0 & 0 & c_{55}(z) & 0 \\ 0 & 0 & 0 & 0 & 0 & c_{66}(z) \end{pmatrix} \begin{pmatrix} \varepsilon_x \\ \varepsilon_y \\ \varepsilon_z \\ \gamma_{yz} \\ \gamma_{xz} \\ \gamma_{xy} \end{pmatrix} - \begin{pmatrix} 0 & 0 & e_{13}(z) \\ 0 & 0 & e_{23}(z) \\ 0 & 0 & e_{33}(z) \\ 0 & e_{24}(z) & 0 \\ e_{15}(z) & 0 & 0 \\ 0 & 0 & 0 \end{pmatrix} \begin{pmatrix} E_x \\ E_y \\ E_z \end{pmatrix} \tag{8a}$$

$$\begin{pmatrix} D_x \\ D_y \\ D_z \end{pmatrix} = \begin{pmatrix} 0 & 0 & 0 & 0 & e_{15}(z) & 0 \\ 0 & 0 & 0 & e_{24}(z) & 0 & 0 \\ e_{13}(z) & e_{23}(z) & e_{33}(z) & 0 & 0 & 0 \end{pmatrix} \begin{pmatrix} \varepsilon_x \\ \varepsilon_y \\ \varepsilon_z \\ \gamma_{yz} \\ \gamma_{xz} \\ \gamma_{xy} \end{pmatrix} + \begin{pmatrix} \mu_{11}(z) & 0 & 0 \\ 0 & \mu_{22}(z) & 0 \\ 0 & 0 & \mu_{33}(z) \end{pmatrix} \begin{pmatrix} E_x \\ E_y \\ E_z \end{pmatrix} \tag{8b}$$

where $\{D\}$ is electric displacement field and c_{ij} $(i,j = 1,2,3,4,5,6)$ are the elastic constants under constant electric field (Zenkour and Alghanmi, 2018) which can be given as follows:

$$c_{11}(z) = c_{22}(z) = c_{33}(z) = \frac{E(z)(1-\nu(z)^2)}{1-3\nu(z)^2-2\nu(z)^2} \tag{9a}$$

$$c_{12}(z) = c_{13}(z) = c_{23}(z) = \frac{E(z)\nu(z)\big(1+\nu(z)\big)}{1-3\nu(z)^2-2\nu(z)^2} \tag{9b}$$

$$c_{44}(z) = c_{55}(z) = c_{66}(z) = \frac{E(z)}{2(1+\nu(z))} \tag{9c}$$

As this is an FGM system, all elastic and piezo coefficients such as elastic modulus (E), Poisson ratio (ν), piezoelectric (e_{ij}) and dielectric (μ_{ij}) coefficients are varying along the direction of the plate thickness (z).

The governing equations for the present static FGPM system are achieved from the principle of virtual displacements that can be given as follows:

$$\int_{t_i}^{t_f} [-(\delta U) + \delta W_{ext}]\, dt = 0 \tag{10a}$$

The virtual strain energy (δU) is expressed as follows:

$$\delta U = \int_0^a \int_0^b \int_{-\frac{h}{2}}^{\frac{h}{2}} \big(\sigma_{xx}\delta\varepsilon_{xx} + \sigma_{yy}\delta\varepsilon_{yy} + \sigma_{zz}\delta\varepsilon_{zz} + \sigma_{xy}\delta\gamma_{xy} + \sigma_{yz}\delta\gamma_{yz} + \sigma_{xz}\delta\gamma_{xz}\big) dxdydz \tag{10b}$$

The virtual work done by the externally applied uniform transverse load p_0 and externally applied Electric potential, V can be written as follows:

$$\delta W_{ext} = \int_0^a \int_0^b [\, p_0(x,y)\delta w_0]\, dxdy + \int_0^a \int_0^b \int_{-\frac{h}{2}}^{\frac{h}{2}} \big[\, D_x\delta E_x + D_y\delta E_y + D_z\delta E_z\big] dxdydz \tag{10c}$$

After substituting the strain-displacement relations and rearranging Eq. (10a), the following six governing equations of motion can be obtained:

$$\frac{\partial N_x}{\partial x} + \frac{\partial N_{xy}}{\partial y} = 0 \tag{11a}$$

$$\frac{\partial N_{xy}}{\partial x} + \frac{\partial N_y}{\partial y} = 0 \tag{11b}$$

$$\frac{\partial^2 M_x}{\partial x^2} + 2\frac{\partial^2 M_{xy}}{\partial x\,\partial y} + \frac{\partial^2 M_y}{\partial y^2} + p_0(x,y) = 0 \tag{11c}$$

$$\frac{\partial^2 P_x}{\partial x^2} + 2\frac{\partial^2 P_{xy}}{\partial x\,\partial y} + \frac{\partial^2 P_y}{\partial y^2} + \frac{\partial Q_x}{\partial x} + \frac{\partial Q_y}{\partial y} + p_0(x,y) = 0 \tag{11d}$$

$$\frac{\partial Q_x}{\partial x}+\frac{\partial Q_y}{\partial y}-Q_z=0 \tag{11e}$$

$$\sum_{k=1}^{N_L}\int_{z_{k-1}}^{z_k}\left[f_2(z)\frac{\partial D_x}{\partial x}+f_2(z)\frac{\partial D_y}{\partial y}-f_2'(z)D_z\right]dz=0 \tag{11f}$$

Here N_{ij}, M_{ij}, P_{ij} are the function (stress and moment) resultants whose definitions are given as follows:

$$\{N_x, N_{xy}, N_y\}=\int_{-\frac{h}{2}}^{\frac{h}{2}}\{\sigma_x,\tau_{xy},\sigma_y\}dz=\sum_{k=1}^{N_L}\int_{z_{k-1}}^{z_k}\{\sigma_x^k,\tau_{xy}^k,\sigma_y^k\}dz \tag{12a}$$

$$\{M_x, M_{xy}, M_y\}=\int_{-\frac{h}{2}}^{\frac{h}{2}}\{\sigma_x,\tau_{xy},\sigma_y\}zdz=\sum_{k=1}^{N_L}\int_{z_{k-1}}^{z_k}\{\sigma_x^k,\tau_{xy}^k,\sigma_y^k\}zdz \tag{12b}$$

$$\{P_x, P_{xy}, P_y\}=\int_{-\frac{h}{2}}^{\frac{h}{2}}\{\sigma_x,\tau_{xy},\sigma_y\}f_1(z)dz=\sum_{k=1}^{N_L}\int_{z_{k-1}}^{z_k}\{\sigma_x^k,\tau_{xy}^k,\sigma_y^k\}f_1(z)dz \tag{12c}$$

$$\{Q_x, Q_y, Q_z\}=\int_{-\frac{h}{2}}^{\frac{h}{2}}\{f_2(z)\tau_{yz}^k, f_2(z)\tau_{xz}^k, f_2'(z)\sigma_z^k\}dz=\sum_{k=1}^{N_L}\int_{z_{k-1}}^{z_k}\{f_2(z)\tau_{yz}^k, f_2(z)\tau_{xz}^k, f_2'(z)\sigma_z^k\}dz \tag{12d}$$

Now if we substitute Eq. (8) in the aforementioned resultants and perform tabulation in the terms of ($\varepsilon_x^0, \varepsilon_y^0$, , $\gamma_{xy}^0, \kappa_x, \kappa_y, \kappa_{xy}, \eta_x, \eta_y, \eta_{xy}, \gamma_{yz}^0, \gamma_{xz}^0, \varphi_z$), we get the following matrix.

$$\begin{pmatrix}N_x\\N_y\\N_{xy}\\M_x\\M_y\\M_{xy}\\P_x\\P_y\\P_{xy}\\Q_z\\Q_y\\Q_x\end{pmatrix}=\begin{pmatrix}A_{11}&A_{12}&0&B_{11}&B_{12}&0&B_{11}^a&B_{12}^a&0&E_{13}\\A_{12}&A_{22}&0&B_{12}&B_{22}&0&B_{12}^a&B_{22}^a&0&E_{23}\\0&0&A_{66}&0&0&B_{66}&0&0&B_{66}^a&0\\B_{11}&B_{12}&0&D_{11}&D_{12}&0&D_{11}^a&D_{12}^a&0&H_{13}\\B_{12}&B_{22}&0&D_{12}&D_{22}&0&D_{12}^a&D_{22}^a&0&H_{23}\\0&0&B_{66}&0&0&D_{66}&0&0&D_{66}^a&0\\B_{11}^a&B_{12}^a&0&D_{11}^a&D_{12}^a&0&F_{11}&F_{12}&0&H_{13}^a\\B_{12}^a&B_{22}^a&0&D_{12}^a&D_{22}^a&0&F_{12}&F_{22}&0&H_{23}^a\\0&0&B_{66}^a&0&0&D_{66}^a&0&0&F_{66}&0\\E_{13}&E_{23}&0&H_{13}&H_{23}&0&H_{13}^a&H_{23}^a&0&G_{33}\\0&0&0&0&0&0&0&0&A_{44}^a&0\\0&0&0&0&0&0&0&0&0&A_{55}^a\end{pmatrix}\begin{pmatrix}\varepsilon_x^0\\\varepsilon_y^0\\\gamma_{xy}^0\\\kappa_x\\\kappa_y\\\kappa_{xy}\\\eta_x\\\eta_y\\\eta_{xy}\\\varphi_z\\\gamma_{yz}^0\\\gamma_{xz}^0\end{pmatrix}-\int_{-\frac{h}{2}}^{\frac{h}{2}}\begin{pmatrix}e_{13}E_z\\e_{23}E_z\\0\\e_{13}zE_z\\e_{23}zE_z\\0\\e_{13}f_1(z)E_z\\e_{23}f_1(z)E_z\\0\\f_2'(z)e_{33}E_z\\e_{24}f_2(z)E_y\\e_{15}f_2(z)E_x\end{pmatrix}dz \tag{13}$$

In Eq. (13), the stiffness coefficients can be defined by

$$\begin{pmatrix} A_{ij} \\ B_{ij} \\ D_{ij} \\ E_{ij} \\ F_{ij} \\ H_{ij} \\ G_{ij} \\ A^{a}_{ij} \\ B^{a}_{ij} \\ D^{a}_{ij} \\ H^{a}_{ij} \end{pmatrix} = \int_{-\frac{h}{2}}^{\frac{h}{2}} \begin{pmatrix} c_{ij} \\ zc_{ij} \\ z^2c_{ij} \\ f_2'(z)c_{ij} \\ f_1^2(z)c_{ij} \\ f_2'(z)zc_{ij} \\ f_2'^2(z)c_{ij} \\ f_2^2(z)c_{ij} \\ f_1(z)c_{ij} \\ f_1(z)zc_{ij} \\ f_2'(z)f_1(z)c_{ij} \end{pmatrix} dz = \sum_{k=1}^{N_L} \int_{z_{k-1}}^{z_k} \begin{pmatrix} c_{ij}^{k} \\ zc_{ij}^{k} \\ z^2c_{ij}^{k} \\ f_2'(z)c_{ij}^{k} \\ f_1^2(z)c_{ij}^{k} \\ f_2'(z)zc_{ij}^{k} \\ f_2'^2(z)c_{ij}^{k} \\ f_2^2(z)c_{ij}^{k} \\ f_1(z)c_{ij}^{k} \\ f_1(z)zc_{ij}^{k} \\ f_2'(z)f_1(z)c_{ij}^{k} \end{pmatrix} dz \qquad ,(i = 1,2,\dots,6) \tag{14}$$

2.4 Governing equations

Putting Eq. (13) in the governing Eq. (11), we get the following six partial differential equations.

$$A_{11}\frac{\partial^2 u_0}{\partial x^2} + A_{66}\frac{\partial^2 u_0}{\partial y^2} + (A_{12} + A_{66})\frac{\partial^2 v_0}{\partial x\,\partial y} - B_{11}\frac{\partial^3 w_{0b}}{\partial x^3} - (B_{12} + 2B_{66})\frac{\partial^3 w_{0b}}{\partial x\,\partial y^2} - B^{a}_{11}\frac{\partial^3 w_{0s}}{\partial x^3} - (B^{a}_{12} + 2B^{a}_{66})\frac{\partial^3 w_{0s}}{\partial x\,\partial y^2} + E_{13}\frac{\partial \varphi_z}{\partial x} + \bar{A}^{p}_{13}\frac{\partial \phi}{\partial x} = 0 \tag{15a}$$

$$A_{66}\frac{\partial^2 v_0}{\partial x^2} + A_{22}\frac{\partial^2 v_0}{\partial y^2} + (A_{12} + A_{66})\frac{\partial^2 u_0}{\partial x\,\partial y} - B_{22}\frac{\partial^3 w_{0b}}{\partial y^3} - (B_{12} + 2B_{66})\frac{\partial^3 w_{0b}}{\partial x^2\,\partial y} - B^{a}_{22}\frac{\partial^3 w_{0s}}{\partial y^3} - (B^{a}_{12} + 2B^{a}_{66})\frac{\partial^3 w_{0s}}{\partial x^2\,\partial y} + E_{23}\frac{\partial \varphi_z}{\partial y} + \bar{A}^{p}_{23}\frac{\partial \phi}{\partial y} = 0 \tag{15b}$$

$$B_{11}\frac{\partial^3 u_0}{\partial x^3} + (B_{12} + 2B_{66})\left(\frac{\partial^3 u_0}{\partial x\,\partial y^2} + \frac{\partial^3 v_0}{\partial x^2\,\partial y}\right) + B_{22}\frac{\partial^3 v_0}{\partial y^3} - D_{11}\frac{\partial^4 w_{0b}}{\partial x^4} - D_{22}\frac{\partial^4 w_{0b}}{\partial y^4} - (2D_{12} + 4D_{66})\frac{\partial^4 w_{0b}}{\partial x^2\,\partial y^2} - D^{a}_{11}\frac{\partial^4 w_{0s}}{\partial x^4} - D^{a}_{22}\frac{\partial^4 w_{0s}}{\partial y^4} - (2D^{a}_{12} + 4D^{a}_{66})\frac{\partial^4 w_{0s}}{\partial x^2\,\partial y^2} + H_{13}\frac{\partial^2 \varphi_z}{\partial x^2} + H_{23}\frac{\partial^2 \varphi_z}{\partial y^2} + p(x,y) + \bar{A}^{zp}_{13}\frac{\partial^2 \phi}{\partial x^2} + \bar{A}^{zp}_{23}\frac{\partial^2 \phi}{\partial y^2} = 0 \tag{15c}$$

$$B^{a}_{11}\frac{\partial^3 u_0}{\partial x^3} + (B^{a}_{12} + 2B^{a}_{66})\left(\frac{\partial^3 u_0}{\partial x\,\partial y^2} + \frac{\partial^3 v_0}{\partial x^2\,\partial y}\right) + B^{a}_{22}\frac{\partial^3 v_0}{\partial y^3} - D^{a}_{11}\frac{\partial^4 w_{0b}}{\partial x^4} - D^{a}_{22}\frac{\partial^4 w_{0b}}{\partial y^4} - (2D^{a}_{12} + 4D^{a}_{66})\frac{\partial^4 w_{0b}}{\partial x^2\,\partial y^2} - F_{11}\frac{\partial^4 w_{0s}}{\partial x^4} - F_{22}\frac{\partial^4 w_{0s}}{\partial y^4} - (2F_{12} + 4F_{66})\frac{\partial^4 w_{0s}}{\partial x^2\,\partial y^2} + A^{a}_{55}\frac{\partial^2 w_{0s}}{\partial x^2} + A^{a}_{44}\frac{\partial^2 w_{0s}}{\partial y^2} + (H^{a}_{13} + A^{a}_{55})\frac{\partial^2 \varphi_z}{\partial x^2} + (H^{a}_{23} + A^{a}_{44})\frac{\partial^2 \varphi_z}{\partial y^2} + p(x,y) + \bar{A}^{fp}_{13}\frac{\partial^2 \phi}{\partial x^2} + \bar{A}^{fp}_{23}\frac{\partial^2 \phi}{\partial y^2} - \underset{\sim}{\bar{A}}^{p}_{24}\frac{\partial^2 \phi}{\partial y^2} - \underset{\sim}{\bar{A}}^{p}_{15}\frac{\partial^2 \phi}{\partial x^2} = 0 \tag{15d}$$

$$-E_{13}\frac{\partial u_0}{\partial x}-E_{23}\frac{\partial v_0}{\partial y}+H_{13}\frac{\partial^2 w_{0b}}{\partial x^2}+H_{23}\frac{\partial^2 w_{0b}}{\partial y^2}+(H_{13}^a+A_{55}^a)\frac{\partial^2 w_{0s}}{\partial x^2}+(H_{23}^a+A_{44}^a)\frac{\partial^2 w_{0s}}{\partial y^2}$$
$$+A_{55}^a\frac{\partial^2\varphi_z}{\partial x^2}+A_{44}^a\frac{\partial^2\varphi_z}{\partial y^2}-G_{33}\varphi_z-\underset{\sim}{\bar{A}}_{24}^p\frac{\partial^2\phi}{\partial y^2}-\underset{\sim}{\bar{A}}_{15}^p\frac{\partial^2\phi}{\partial x^2}+\phi EE_{33}+\frac{2V}{h}\bar{A}_{33}^p=0 \quad (15e)$$

$$\underset{\sim}{\bar{A}}_{15}^p\left(\frac{\partial^2 w_{0s}}{\partial x^2}+\frac{\partial^2\varphi_z}{\partial x^2}\right)+\bar{D}_{11}^p\frac{\partial^2\phi}{\partial x^2}+\underset{\sim}{\bar{A}}_{24}^p\left(\frac{\partial^2 w_{0s}}{\partial y^2}+\frac{\partial^2\varphi_z}{\partial y^2}\right)+\bar{D}_{22}^p\frac{\partial^2\phi}{\partial y^2}+\bar{A}_{13}^p\frac{\partial u_0}{\partial x}+\bar{A}_{23}^p\frac{\partial v_0}{\partial y}$$
$$-\bar{A}_{13}^{zp}\frac{\partial^2 w_{0b}}{\partial x^2}-\bar{A}_{23}^{zp}\frac{\partial^2 w_{0b}}{\partial y^2}-\bar{A}_{13}^{fp}\frac{\partial^2 w_{0s}}{\partial x^2}-\bar{A}_{23}^{fp}\frac{\partial^2 w_{0s}}{\partial y^2}-\bar{H}_{33}^p\phi-\bar{H}_{33}^{pp}V \quad (15f)$$
$$-EE_{33}\varphi_z=0$$

In Eq. (15), EE_{33}, $\bar{A}_{31}^p$, $\bar{A}_{32}^p$, $\bar{A}_{33}^p$, $\bar{A}_{31}^{zp}$, $\bar{A}_{32}^{zp}$, $\underset{\sim}{\bar{A}}_{24}^p$, $\underset{\sim}{\bar{A}}_{15}^p$, $\bar{A}_{31}^{fp}$, $\bar{A}_{32}^{fp}$, $\bar{D}_{11}^p$, $\bar{D}_{22}^p$, $\bar{H}_{33}^p$, $\bar{H}_{33}^{pp}$ which corroborate the piezoelectric coupling coefficients are defined by:

$$EE_{33}=\int_{-\frac{h}{2}}^{\frac{h}{2}}e_{33}(z)f_2'^2(z)dz=\sum_{k=1}^{N_L}\int_{z_{k-1}}^{z_k}e_{33}^k(z)f_2'^2(z)dz \quad (16a)$$

$$\{\bar{A}_{13}^p,\bar{A}_{23}^p,\bar{A}_{33}^p\}=\int_{-\frac{h}{2}}^{\frac{h}{2}}-\{e_{13}(z),e_{23}(z),e_{33}(z)\}f_2'(z)dz$$
$$=\sum_{k=1}^{N_L}\int_{z_{k-1}}^{z_k}-\{e_{13}^k(z),e_{23}^k(z),e_{33}^k(z)\}f_2'(z)dz \quad (16b)$$

$$\{\bar{A}_{13}^{zp},\bar{A}_{23}^{zp}\}=\int_{-\frac{h}{2}}^{\frac{h}{2}}-\{e_{13}(z),e_{23}(z)\}zf_2'(z)dz=\sum_{k=1}^{N_L}\int_{z_{k-1}}^{z_k}-\{e_{13}^k(z),e_{23}^k(z)\}zf_2'(z)dz \quad (16c)$$

$$\left\{\underset{\sim}{\bar{A}}_{24}^p,\underset{\sim}{\bar{A}}_{15}^p\right\}=\int_{-\frac{h}{2}}^{\frac{h}{2}}\{e_{24}(z),e_{15}(z)\}f_2^2(z)dz=\sum_{k=1}^{N_L}\int_{z_{k-1}}^{z_k}\{e_{24}^k(z),e_{15}^k(z)\}f_2^2(z)dz \quad (16d)$$

$$\left\{\bar{A}_{13}^{fp},\bar{A}_{23}^{fp}\right\}=\int_{-\frac{h}{2}}^{\frac{h}{2}}-f_1(z)\{e_{13}(z),e_{23}(z)\}f_2'(z)dz=\sum_{k=1}^{N_L}\int_{z_{k-1}}^{z_k}-f_1(z)\{e_{13}^k(z),e_{23}^k(z)\}f_2'(z)dz \quad (16e)$$

$$\{\bar{D}_{11}^p,\bar{D}_{22}^p\}=\int_{-\frac{h}{2}}^{\frac{h}{2}}\{\mu_{11}(z),\mu_{22}(z)\}f_2^2(z)dz=\sum_{k=1}^{N_L}\int_{z_{k-1}}^{z_k}\{\mu_{11}^k(z),\mu_{22}^k(z)\}f_2^2(z)dz \quad (16f)$$

$$\{\bar{H}_{33}^p,\bar{H}_{33}^{pp}\}=\int_{-\frac{h}{2}}^{\frac{h}{2}}\{\mu_{33}(z)f_2'(z),-\frac{2}{h}\mu_{33}(z)\}f_2'(z)dz=\sum_{k=1}^{N_L}\int_{z_{k-1}}^{z_k}\{\mu_{33}^k(z)f_2'(z),-\frac{2}{h}\mu_{33}^k(z)\}f_2'(z)dz \quad (16g)$$

Here, Navier's method is implemented to get the analytical results, wherein the following boundary constraints of the four ends simply supported (SSSS) plate are assigned.

Edge 1: $y = 0$ $\quad u_0(x,0) = w_{ob}(x,0) = w_{0s}(x,0) = \varphi_z(x,0) = 0$

Edge 2: $y = a$ $\quad u_0(x,a) = w_{ob}(x,a) = w_{0s}(x,a) = \varphi_z(x,a) = 0$

Edge 3: $x = 0$ $\quad v_0(0,y) = w_{ob}(0,y) = w_{0s}(0,y) = \varphi_z(0,y) = 0$

Edge 4: $x = b$ $\quad v_0(b,y) = w_{ob}(b,y) = w_{0s}(b,y) = \varphi_z(b,y) = 0$

To satisfy the aforementioned boundary conditions, $(u_0, v_0, w_{0b}, w_{0s}, \varphi_z)$ are expressed using an infinite series which are given by:

$$u_0(x,y) = \sum_{m=1}^{\infty}\sum_{n=1}^{\infty} U_{mn} \cos\left(\frac{m\pi x}{b}\right) \sin\left(\frac{n\pi y}{a}\right) \tag{17a}$$

$$v_0(x,y) = \sum_{m=1}^{\infty}\sum_{n=1}^{\infty} V_{mn} \sin\left(\frac{m\pi x}{b}\right) \cos\left(\frac{n\pi y}{a}\right) \tag{17b}$$

$$w_{0b}(x,y) = \sum_{m=1}^{\infty}\sum_{n=1}^{\infty} W_{bmn} \sin\left(\frac{m\pi x}{b}\right) \sin\left(\frac{n\pi y}{a}\right) \tag{17c}$$

$$w_{0s}(x,y) = \sum_{m=1}^{\infty}\sum_{n=1}^{\infty} W_{smn} \sin\left(\frac{m\pi x}{b}\right) \sin\left(\frac{n\pi y}{a}\right) \tag{17d}$$

$$\varphi_z(x,y) = \sum_{m=1}^{\infty}\sum_{n=1}^{\infty} \Phi_{mn} \sin\left(\frac{m\pi x}{b}\right) \sin\left(\frac{n\pi y}{a}\right) \tag{17e}$$

As Eq. (15) contains total six primary unknown variables, the mechanical (p_0) and electrical load (ϕ) are also expressed based on double sine series as follows:

$$\phi(x,y) = \sum_{m=1}^{\infty}\sum_{n=1}^{\infty} Y_{mn} \sin\left(\frac{m\pi x}{b}\right) \sin\left(\frac{n\pi y}{a}\right) \tag{17f}$$

$$p_0(x,y) = \sum_{m=1}^{\infty}\sum_{n=1}^{\infty} p_{mn} \sin\left(\frac{m\pi x}{b}\right) \sin\left(\frac{n\pi y}{a}\right) \tag{17g}$$

We consider that a uniform transverse load, p_0 is acting throughout the top surface of the plate. Thus we have $p_0(x,y) = p_0$ and value of p_{mn} can be determined from Fourier series expansion.

$$p_{mn} = \frac{4}{ab}\int_0^a \int_0^b p_0 \sin\left(\frac{m\pi x}{b}\right)\sin\left(\frac{n\pi y}{a}\right) dxdy = \frac{4p_0}{mn\pi^2}(1-\cos m\pi)(1-\cos n\pi) \tag{18}$$

Now, we have to assume a function $V_s(x,y)$ (potential per unit surface) to tackle the external applied electric voltage V in the Eqn. (15e) and (15f). Similar to $p_0(x,y)$, this $V_s(x,y)$ can also be expressed as double sine series as follows.

$$V_s(x,y) = \sum_{m=1}^{\infty}\sum_{n=1}^{\infty} E_{mn}\sin\left(\frac{m\pi x}{b}\right)\sin\left(\frac{n\pi y}{a}\right) \tag{19}$$

Similarly, considering $V_s(x,y) = \frac{V}{ab}$ i.e., independent of x and y, E_{mn} can be determined similar to p_{mn}.

$$E_{mn} = \frac{4V}{mnab\pi^2}(1-\cos m\pi)(1-\cos n\pi) \tag{20}$$

Note here that while we have considered uniformly distributed mechanical load and electrical voltage, other loading conditions can also be analyzed based on the analytical framework presented here. Substituting Eqs. (17), (18), (19) and (20) in the partial differential Eqs. (15), we get the following six linear simultaneous equations of $U_{mn}, V_{mn}, W_{bmn}, W_{smn}, \Phi_{mn}, Y_{mn}$.

$$\begin{aligned}-A_{11}U_{mn}\bar{m}^2 - A_{66}U_{mn}\bar{n}^2 - (A_{12}+A_{66})V_{mn}\bar{m}\bar{n} + B_{11}W_{bmn}\bar{m}^3 + (B_{12}+2B_{66})W_{bmn}\bar{n}^2\bar{m}\\ + B_{11}^a W_{smn}\bar{m}^3 + (B_{12}^a + 2B_{66}^a)W_{smn}\bar{n}^2\bar{m} + E_{13}\Phi_{mn}\bar{m} + \bar{A}_{13}^p Y_{mn}\bar{m} = 0\end{aligned} \tag{21a}$$

$$\begin{aligned}-A_{66}V_{mn}\bar{m}^2 - A_{22}V_{mn}\bar{n}^2 - (A_{12}+A_{66})U_{mn}\bar{m}\bar{n} + B_{22}W_{bmn}\bar{n}^3 + (B_{12}+2B_{66})W_{bmn}\bar{m}^2\bar{n}\\ + B_{22}^a W_{smn}\bar{n}^3 + (B_{12}^a + 2B_{66}^a)W_{smn}\bar{m}^2\bar{n} + E_{23}\Phi_{mn}\bar{n} + \bar{A}_{23}^p Y_{mn}\bar{n} = 0\end{aligned} \tag{21b}$$

$$\begin{aligned}B_{11}U_{mn}\bar{m}^3 + (B_{12}+2B_{66})(U_{mn}\bar{n}^2\bar{m} + V_{mn}\bar{m}^2\bar{n}) + B_{22}V_{mn}\bar{n}^3 - D_{11}W_{bmn}\bar{m}^4 - D_{22}W_{bmn}\bar{n}^4\\ - (2D_{12}+4D_{66})W_{bmn}\bar{m}^2\bar{n}^2 - D_{11}^a W_{smn}\bar{m}^4 - D_{22}^a W_{smn}\bar{n}^4\\ - (2D_{12}^a + 4D_{66}^a)W_{smn}\bar{m}^2\bar{n}^2 - H_{13}\Phi_{mn}\bar{m}^2 - H_{23}\Phi_{mn}\bar{n}^2 + p_{mn} - \bar{A}_{13}^{zp}Y_{mn}\bar{m}^2\\ - \bar{A}_{23}^{zp}Y_{mn}\bar{n}^2 = 0\end{aligned} \tag{21c}$$

$$\begin{aligned}B_{11}^a U_{mn}\bar{m}^3 + (B_{12}^a+2B_{66}^a)(U_{mn}\bar{n}^2\bar{m} + V_{mn}\bar{m}^2\bar{n}) + B_{22}^a V_{mn}\bar{n}^3 - D_{11}^a W_{bmn}\bar{m}^4 - D_{22}^a W_{bmn}\bar{n}^4\\ - (2D_{12}^a + 4D_{66}^a)W_{bmn}\bar{m}^2\bar{n}^2 - F_{11}W_{smn}\bar{m}^4 - F_{22}W_{smn}\bar{n}^4\\ - (2F_{12}+4F_{66})W_{smn}\bar{m}^2\bar{n}^2 - A_{55}^a W_{smn}\bar{m}^2 - A_{44}^a W_{smn}\bar{n}^2 - (H_{13}^a + A_{55}^a)\Phi_{mn}\bar{m}^2\\ - (H_{23}^a + A_{44}^a)\Phi_{mn}\bar{n}^2 + p_{mn} - \bar{A}_{13}^{fp}Y_{mn}\bar{m}^2 - \bar{A}_{23}^{fp}Y_{mn}\bar{n}^2 + \underset{\sim}{\bar{A}}_{24}^{p}\, Y_{mn}\bar{n}^2\\ + \underset{\sim}{\bar{A}}_{15}^{p}\, Y_{mn}\bar{m}^2 = 0\end{aligned} \tag{21d}$$

$$E_{13}U_{mn}\bar{m} + E_{23}V_{mn}\bar{n} - H_{13}W_{bmn}\bar{m}^2 - H_{23}W_{bmn}\bar{n}^2 - (H_{13}^a + A_{55}^a)W_{smn}\bar{m}^2 - (H_{23}^a + A_{44}^a)W_{smn}\bar{n}^2 - A_{55}^a\Phi_{mn}\bar{m}^2 - A_{44}^a\Phi_{mn}\bar{n}^2 - G_{33}\Phi_{mn} + \underset{\sim}{\bar{A}}_{24}^{p} Y_{mn}\bar{n}^2 + \underset{\sim}{\bar{A}}_{15}^{p} Y_{mn}\bar{m}^2 + EE_{33}Y_{mn} + \frac{2E_{mn}}{h}\bar{A}_{33}^{p} = 0 \quad (21e)$$

$$\underset{\sim}{\bar{A}}_{15}^{p}(-W_{smn}\bar{m}^2 - \Phi_{mn}\bar{m}^2) - \bar{D}_{11}^{p}Y_{mn}\bar{m}^2 - \underset{\sim}{\bar{A}}_{24}^{p}(-W_{smn}\bar{n}^2 - \Phi_{mn}\bar{n}^2) - \bar{D}_{22}^{p}Y_{mn}\bar{n}^2 - \bar{A}_{13}^{p}U_{mn}\bar{m} - \bar{A}_{23}^{p}V_{mn}\bar{n} + \bar{A}_{13}^{zp}W_{bmn}\bar{m}^2 + \bar{A}_{23}^{zp}W_{bmn}\bar{n}^2 + \bar{A}_{13}^{fp}W_{smn}\bar{m}^2 + \bar{A}_{23}^{fp}W_{smn}\bar{n}^2 - \bar{H}_{33}^{p}Y_{mn} - \bar{H}_{33}^{pp}E_{mn} - EE_{33}\Phi_{mn} = 0 \quad (21f)$$

Here $(\bar{m}, \bar{n}) = \left(\frac{m\pi}{b}, \frac{n\pi}{a}\right)$. Solving six simultaneous Eqs. (21), we can determine $W_{bmn}, W_{smn}, \Phi_{mn}$ and accordingly, the total transverse deflection $w(x, y, z)$ of the plate can be calculated by adding these three effects of bending, shear and stretching. By solving for Y_{mn}, we can calculate the voltage component corresponding to the applied load. It can be noted in this context that the above formulation is valid for single and multi-layer (with the number of layers N_L) functionally graded plates. Equivalent material properties are adopted for utilizing the analytical framework presented here as described below.

2.5 Equivalent material properties

The PVDF has isotropic and piezoelectric properties, and it is presumed that GPLs are uniformly and linearly distributed with a randomly distributed placement within the PVDF matrix. Such randomly oriented fiber composite can be approximated to a quasi-isotropic laminate (Halpin and Karoos, 1978). Here the GPLs are assumed as rectangular-shaped solid reinforcement of average width w_{GPL}, length l_{GPL} and thickness t_{GPL}. The electromechanical behaviour of the FGPM plate is discussed by considering two distributions of weight fraction of GPLs along the thickness direction (z) which are as follows (Zhao et al., 2020):

- Linear distribution: $W_{GPL}(z) = 200W_{GPL}^{*}\left(\frac{1}{2} + \frac{z}{h}\right)W_{GPL}^{0}$ (22a)
- Uniform distribution: $W_{GPL}(z) = 100W_{GPL}^{*}W_{GPL}^{0}$ (22b)

where W_{GPL}^{*} and W_{GPL}^{0} are the total weight fraction and characteristic value of GPLs weight fraction, respectively. The total volume fraction of GPLs is calculated using the following relation:

$$V_{GPL}(z) = \frac{W_{GPL}(z)}{W_{GPL}(z) + \left(\frac{\rho_{GPL}}{\rho_{PVDF}}\right)(1 - W_{GPL}(z))} \quad (23)$$

where ρ_{GPL} and ρ_{PVDF} denote the respective mass densities of GPLs and PVDF matrix. The modified Halpin-Tsai model is utilised to estimate the effective material constants (properties). The Young modulus of a nearly isotropic laminate system is as follows (Wang et al., 2020):

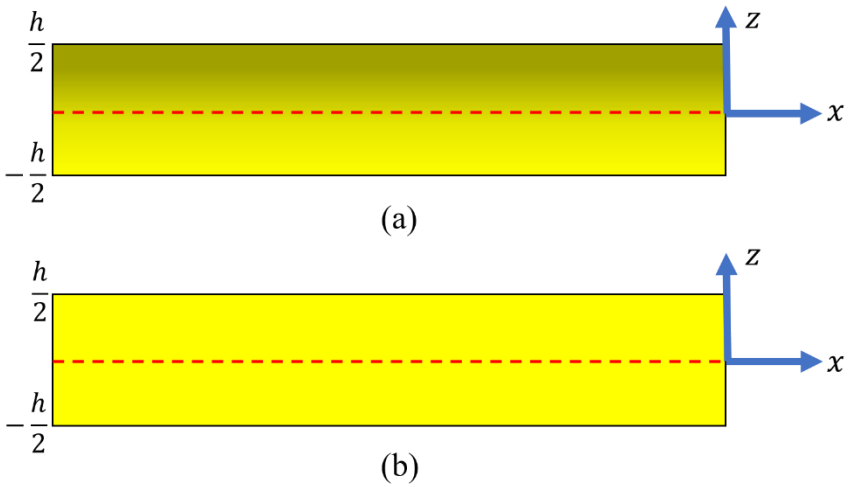

Fig. 3. Distribution of W_{GPL} across the thickness of single-layered FGPM (x–z plane) **(a)** linear and **(b)** uniform distribution.

$$E(z) = \frac{3}{8}E_L + \frac{5}{8}E_T \tag{24}$$

whereas E_L and E_T indicate the longitudinal and transverse moduli and their values can be estimated from the Eq. (25). Here $\frac{3}{8}$ and $\frac{5}{8}$ are the reinforcing efficiency of GPLs considered in longitudinal and transverse directions, respectively.

$$\{E_L(z), E_T(z)\} = \left\{\frac{1+\xi_L^{GPL}\eta_L^{GPL}V_{GPL}(z)}{1-\eta_L^{GPL}V_{GPL}(z)}, \frac{1+\xi_W^{GPL}\eta_W^{GPL}V_{GPL}(z)}{1-\eta_W^{GPL}V_{GPL}(z)}\right\}E_{PVDF} \tag{25}$$

where the parameters η_L^{GPL} and η_W^{GPL} can be expressed by

$$\{\eta_L^{GPL}, \eta_W^{GPL}\} = \left\{\frac{\left(\frac{E_{GPL}}{E_{PVDF}}\right)-1}{\left(\frac{E_{GPL}}{E_{PVDF}}\right)+\xi_L^{GPL}}, \frac{\left(\frac{E_{GPL}}{E_{PVDF}}\right)-1}{\left(\frac{E_{GPL}}{E_{PVDF}}\right)+\xi_W^{GPL}}\right\} \tag{26}$$

Here E_{GPL} and E_{PVDF} indicate the respective Young moduli of GPLs and PVDF matrix, and filler geometric factors ξ_L^{GPL} and ξ_W^{GPL} of GPLs are given by the following equations:

$$\left\{\xi_L^{GPL}, \xi_w^{GPL}\right\} = \left\{\frac{2l_{GPL}}{t_{GPL}}, \frac{2w_{GPL}}{t_{GPL}}\right\} \tag{27}$$

where t_{GPL}, l_{GPL}, and w_{GPL} are the respective thickness, length, and width of GPLs fillers. Other material properties are calculated by the rule of mixture which is as follows:

$$\rho(z) = \rho_{GPL}V_{GPL}(z) + \rho_{PVDF}(1 - V_{GPL}(z)) \tag{28a}$$

$$\nu(z) = \nu_{GPL}V_{GPL}(z) + \nu_{PVDF}(1 - V_{GPL}(z)) \quad (28b)$$

$$[e_{ij}(z)] = \alpha[e_{3i}]^{PVDF}V_{GPL}(z) + [e_{3i}]^{PVDF}(1 - V_{GPL}(z)) \quad (28c)$$

$$[k_{ii}(z)] = \alpha[k_{ii}]^{PVDF}V_{GPL}(z) + [k_{ii}]^{PVDF}(1 - V_{GPL}(z)) \quad (28d)$$

where ν, e_{ij} $(i,j = 1,2,3,4,5)$, $k_{ii}(i = 1,2,3)$ and α are the Poison ratio, coupling coefficient, electric permittivity and piezoelectric multiple, respectively. Table 1 summarizes the values of all these coefficients.

Table 1: Geometric and material properties of constituents of FGPM (Li et al., 2020)

Elastic and geometrical properties		**Piezoelectric constants** (C/m^2)	
W_{GPL}^0	1%	e_{31}^{PVDF}	32.075×10^{-3}
l_{GPL}	2.5μm	e_{32}^{PVDF}	-4.07×10^{-3}
w_{GPL}	1.5μm	e_{33}^{PVDF}	-21.19×10^{-3}
t_{GPL}	1.5nm	e_{24}^{PVDF}	-12.65×10^{-3}
α	100×1000	e_{15}^{PVDF}	-15.93×10^{-3}
ρ_{GPL}	1920 kg/m^3	**Dielectric constants** (F/m)	
ρ_{PVDF}	800 kg/m^3	μ_{11}^{PVDF}	53.985×10^{-12}
E_{GPL}	1010 GPa	μ_{22}^{PVDF}	66.375×10^{-12}
E_{PVDF}	1.44 GPa	μ_{33}^{PVDF}	59.295×10^{-12}
ν_{GPL}	0.186		
ν_{PVDF}	0.29		

2.6 Time-dependent viscoelastic analysis

Here the analytical model presented in the preceding sections has been extended for analyzing the functionally graded piezoelectric plates with time-dependent viscoelastic properties. For the sake of simplicity, the complex elastic modulus of the plate in the frequency domain (ω) is expressed as the Biot's viscoelactic model with only one term (Mukhopadhyay et al., 2019).

$$E_z^*(\omega) = E'(\omega) + iE''(\omega) = E(z)\left(1 + \epsilon\frac{i\omega}{\mu + i\omega}\right) \quad (29)$$

where $E(z)$ is the effective young modulus in the absence of viscoelasticity, given in Eq. 24 and $i = \sqrt{-1}$. ϵ and μ are the constants indicating "the strength" of viscosity and relaxation parameter respectively. E' (real

part) and E''(imaginary part) can be regarded as storage and loss modulus respectively. The amplitude (dynamic modulus) and phase of the complex modulus can be derived as follows:

$$|E_z^*(\omega)| = E(z)\sqrt{\frac{\mu^2 + \omega^2(1+\epsilon)^2}{\mu^2 + \omega^2}} \tag{30a}$$

$$\phi\left(E_z^*(\omega)\right) = \tan^{-1}\left(\frac{\epsilon\mu\omega}{\mu^2 + \omega^2 + \epsilon\omega^2}\right) \tag{30b}$$

As the phase increases, the contribution of loss modulus will increase which in turn makes the material more viscous (Mun et al., 2007). Considering all the limiting properties of $E_z^*(\omega)$, present in the existing literature, it can be deduced that for all positive ω and ϵ, $|E_z^*(\omega)|$ achieves minimum amplitude ($E(z)$) when $\omega \to 0$ and $\mu \to \infty$ whereas the same will achieve maximum amplitude ($E(z)(1+\epsilon)$) when $\omega \to \infty$ and $\mu \to 0$. However, for all limiting cases, the viscoelastic material properties tend to be pure elastic as the phase $\phi\left(E_z^*(\omega)\right)$ becomes zero.

To employ this complex modulus in the present analytic model and for capturing the realistic time-dependent viscoelastic behaviour of the plate, it is necessary to invert back the frequency domain representation discussed above into the time-domain (t). This inversion of young modulus from its frequency domain (refer Eq. 29) to the time domain is carried out by the efficient inverse Fourier algorithm written in MATLAB symbolic environment. All values of ω, from highest to lowest, are taken into account when inverting frequency domain data into the time domain ($t > 0$). This inversion can be expressed as follows:

$$E_z(t) = \frac{1}{2\pi}\int_{-\infty}^{\infty} E_z^*(\omega)e^{i\omega t}d\omega = \int_{-\infty}^{\infty} E_z^*(2\pi f)e^{2\pi f i t}d\omega \tag{31}$$

Here the function $E_z(t)$ (also called relaxation modulus) encompasses the thickness direction (z) along with the time parameter (t). Handling these two parameters at the same time in the present analytical model can be cumbersome. To mitigate this issue, we have performed the temporal analysis throughout the plate thickness at each time step separately. The evolution of material properties at each time step is determined by a suitable viscoelasticity model. Note that the FE validations (comparative results obtained from the analytical approach and FEM) presented in this paper can be regarded as the validation for a particular time step and the corresponding material properties in the context of time-dependent viscoelastic analysis. By ensuring the accuracy of results at each time step corresponding to time-dependent material properties obtained based on suitable viscoelastic models, the correctness of the overall temporal analysis is ascertained. In this context, it can be noted that two viscoelastic parameters (μ and ϵ) need to be evaluated specific to the material under consideration. The time-dependent variation of material properties depends on these parameters.

We approximate the integral in Eq. (14) by taking a summation through the plate's thickness for each time instant. As here some approximations are involved, the accuracy of the result is ensured by comparing the value of each constant in Eq. (14) obtained from the present summation method and the normal integral method at a particular time instant. Considering time-domain, Eq. (17a-f) can be rewritten as follows:

$$u_0(x,y,t) = \sum_{m=1}^{\infty}\sum_{n=1}^{\infty} U_{mn}(t)\cos\left(\frac{m\pi x}{b}\right)\sin\left(\frac{n\pi y}{a}\right) \tag{32a}$$

$$v_0(x,y,t) = \sum_{m=1}^{\infty}\sum_{n=1}^{\infty} V_{mn}(t)\sin\left(\frac{m\pi x}{b}\right)\cos\left(\frac{n\pi y}{a}\right) \tag{32b}$$

$$w_{0b}(x,y,t) = \sum_{m=1}^{\infty}\sum_{n=1}^{\infty} W_{bmn}(t)\sin\left(\frac{m\pi x}{b}\right)\sin\left(\frac{n\pi y}{a}\right) \tag{32c}$$

$$w_{0s}(x,y,t) = \sum_{m=1}^{\infty}\sum_{n=1}^{\infty} W_{smn}(t)\sin\left(\frac{m\pi x}{b}\right)\sin\left(\frac{n\pi y}{a}\right) \tag{32d}$$

$$\varphi_z(x,y,t) = \sum_{m=1}^{\infty}\sum_{n=1}^{\infty} \Phi_{mn}(t)\sin\left(\frac{m\pi x}{b}\right)\sin\left(\frac{n\pi y}{a}\right) \tag{32e}$$

$$\phi(x,y,t) = \sum_{m=1}^{\infty}\sum_{n=1}^{\infty} Y_{mn}(t)\sin\left(\frac{m\pi x}{b}\right)\sin\left(\frac{n\pi y}{a}\right) \tag{32f}$$

Afterwards, solving Eq. (21) in conjunction with Eq. (32), the time-dependent parameters $W_{bmn}(t), W_{smn}(t), \Phi_{mn}(t)$ can be calculated for each time instant. Thus, in the proposed framework of viscoelastic analysis, we first characterize the frequency-domain depth-wise material properties, which are then inverted to time-domain variation of the depth-wise varying material properties and subsequently used to analyze the electromechanical response of the plates at each time-step.

3. Finite element (FE) analysis

We have carried out a separate finite element analysis to validate the analytical framework as described in the preceding section. The primary objective of including the finite element model in present paper is to give an initial validation to our parent general analytic model (which is equally applicable for both viscoelastic and non-viscoelastic structures). The elastic model, for which we have presented finite element validations, is further extended to analyze the viscoelastic behavior where only the elastic modulus terms in the analytical expressions are replaced by the viscoelastic parameters based on the correspondence principle. The essence of

this principle is that the analytical expressions of the structure in the elastic regime can be readily extended to the viscoelastic regime without any further change in the parent elastic framework. It is well-established in the literature that a correct elastic framework for analyzing structural behaviour can be converted to time-dependent viscoelastic analysis through this principle. The FEM analysis presented in the current paper is intended to establish the accuracy of the elastic analysis, which in turn assures the correctness of the viscoelastic analysis. That is why no additional FE calculations are added for viscoelastic structures separately. In this context, it can be noted that the FE validations presented here can be regarded as the validation for a particular time step and the corresponding material properties in the context of time-dependent viscoelastic analysis. Once the electromechanical analysis is validated for a particular set of material properties, it can be extended to the other time steps readily by considering the appropriate time-dependent material properties at different other time steps. Thus finite element validation of the electromechanical analysis for a particular set of material properties, as presented here, is sufficient for the time-dependent viscoelastic analysis performed afterwards in this study.

The finite element analysis is carried out here considering single and multi-layered systems, wherein the equivalent material properties are evaluated based on the approach presented in the preceding section. The same geometry and the coordinate system are adopted in FE analysis as shown in Fig. 2. The CAD model is prepared in the COMSOL multi-physics version 5.5 software package and FEM simulation has been performed in COMSOL's 3D "piezoelectricity multiphysics interface" which combines Solid Mechanics and Electrostatics together with the constitutive relationships required to model piezoelectrics. In the geometry, thickness direction is taken along the *z*-axis and material coordinate system are same as the spatial coordinate system in COMSOL. For simulating FGPM (functionally graded piezoelectric material) in the present structure, we have created a "blank material" within COMSOL material library whose elastic and piezoelectric properties are given in accordance with Eqns. (24) and (28). As all the properties vary along the thickness direction, we have adopted the COMSOL's global coordinate variable z with lower limit of $-h/2$ and upper limit of $h/2$ to build the analytic functions for its material properties (density, elasticity matrix, coupling matrix and relative permittivity matrix). The discretization of the rectangular plate is carried out using free tetrahedral (tet) mesh (fine) elements where the maximum element size varies between 0.24 m to 0.03 m.

As the analysis is performed on an electromechanical structure, we have to incorporate electrical boundary conditions in addition to mechanical loadings. Present FGPM rectangular plate is under the closed-circuit condition where initially, the electric potential V applied on the upper and lower surfaces are expected to be zero (grounded) throughout the analysis (as demonstrated in Fig. 4). In COMSOL, the piezoelectric polarization axis is not changed as its default direction is always along its spatial z coordinate axis. In case of mechanical loading, a uniformly distributed (UDL) unit force is applied throughout the top surface and the bottom surface is kept free. The plate is modeled as simply supported along four edges (SSSS). The overall FE

Table 2: Initial dimensions of the plate.

Parameters	Values	Unit
Length, b	3	m
Width, a	1	m
Thickness to span ratio (h/a)	0.01	-
Total No. of layer, N_L	• Single (= 1) • multilayer (> 1)	-

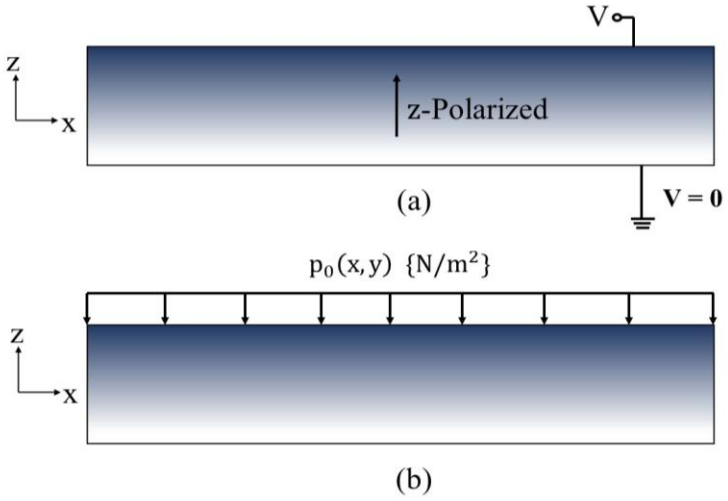

Fig. 4. Schematic representation of FGPM plate su bjected to: **(a)** electrical **(b)** mechanical loads.

modeling is demonstrated using a flow diagram in Fig. 5. In this context, it can be noted that the finite element validations presented here can be regarded as the validation for a typical time step considering the corresponding material properties. In time-dependent viscoelastic analysis, the material properties vary at different time steps that can be ascertained by the adopted viscoelastic model. Once the electromechanical analysis is validated for a particular set of material properties, it can be extended to the other time steps readily by considering the appropriate time-dependent material properties at different other time steps. The time-dependent evolution of material properties in a viscoelastic analysis is discussed in the preceding section.

4. Results and discussions

This section presents numerical results concerning the electromechanical behavior of FGPM plates based on the proposed analytical approach and comparative validation results using finite element simulations. We would investigate three different configurations with single and multiple layers (UD, LD and UD/LD). Subsequently, we present time-dependent viscoelastic results for the deformation and electric potential of FGPM plates.

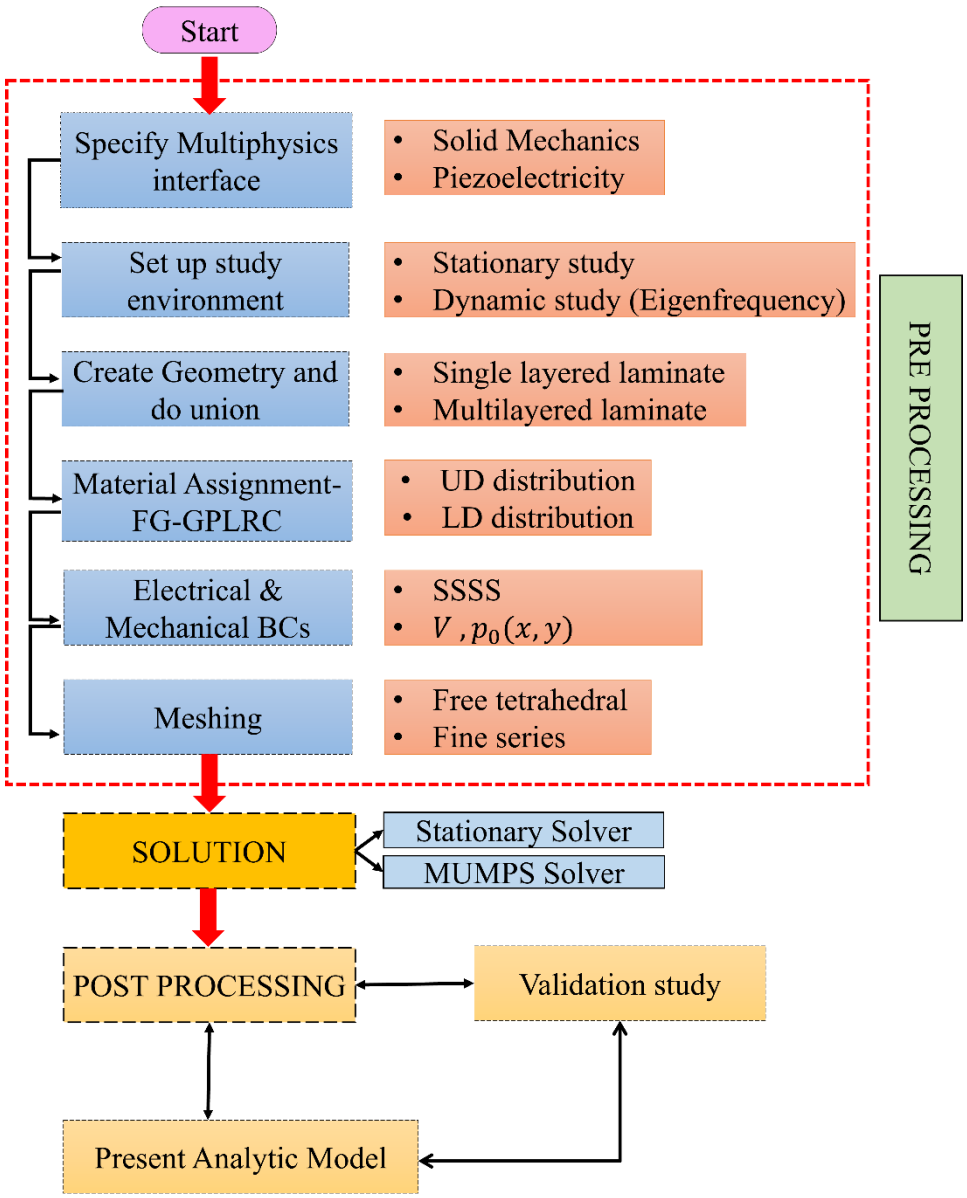

Fig. 5. Flowchart describing the detailed FE analysis.

4.1 Electromechanical analysis of single FGPM plate ($N_L = 1$)

A thin FGM plate ($a/h = 100$) is subjected to uniformly distributed load ($p_0 = 1\ N/m^2$) while it's all four edges are kept simply supported. We first concentrate on validating the analytical model using separate FE analysis, wherein a convergence study is important to obtain credible results before proceeding further. Therefore, the convergence study concerning FE analysis is carried out to investigate the influence of mesh size or the number of elements on the transverse deflection of the plate. Different types of meshing such as: extreme coarse, coarse, normal, fine and extreme fine are considered with the overall range of average element size between 0.855 m to 0.0303 m. In Table 3, the results of convergence study with respect to maximum center deflection of the plate and its mesh statistics used in FE analysis have been presented. Figure 6 illustrates the variation of transverse deflection of the plate over its length. It can be observed that the results for transverse

Table 3: Convergence study of FEM for Center deflection of Plate

Mesh Type	Number of Domain Element	Number of Boundary Element	Number of Edge Element	Plate Center Deflection (μm)
Extreme coarse	597	476	92	-21.966
Coarse	3196	2268	212	-32.929
Normal	7486	5252	312	-33.123
Fine	24560	16340	548	-33.199
Extreme Fine	301244	142524	1604	-33.200

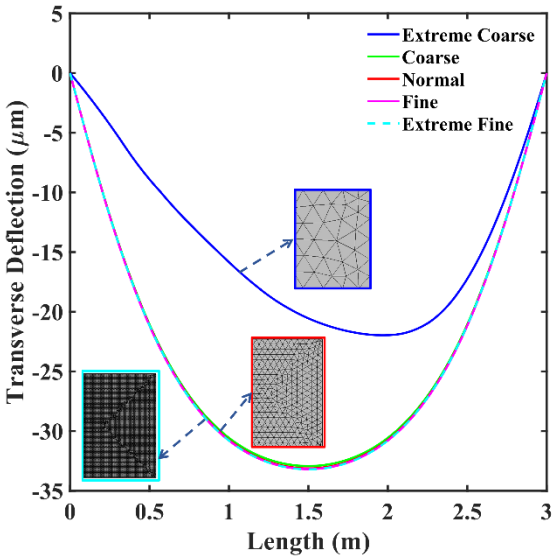

Fig. 6. Mesh convergence analysis.

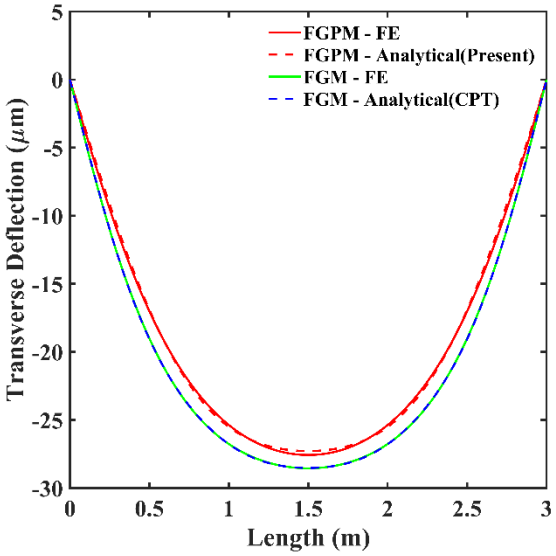

Fig. 7. Variation of transverse deflection of UD FGM plates along its length based on analytical and FE models.

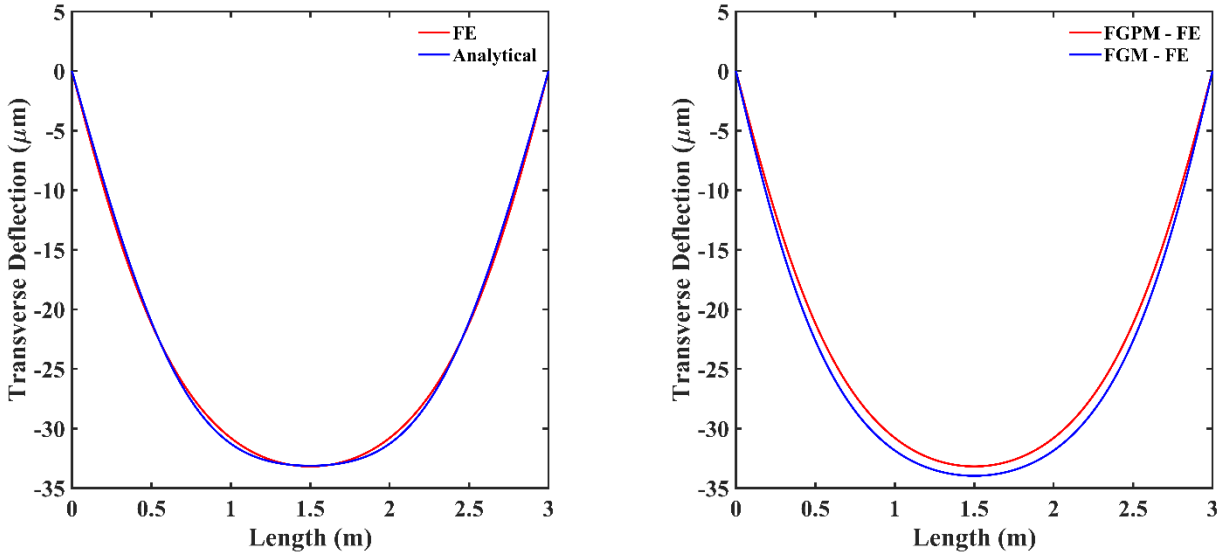

(a) (b)

Fig. 8. (a) Variation of transverse deflection of SSSS FGPM plate along its length (LD case; $a/h = 100, W^*_{GPL} = 1\%, V = 0, p_0 = 1$). **(b)** Variation of transverse deflection of LD plates along its length.

deformations are converged for fine and extreme fine elements. Therefore, we followed the 'fine' type of element for further analysis in FE modeling.

We further validate the FE model with literature to ensure its prediction accuracy. Figure 7 demonstrates the variation of transverse deflection of SSSS FGPM and FGM plates (i.e., with and without accounting for the piezoelectric effect) over their lengths and a comparison of the available results based on classical plate theory (CPT) (Reddy, 2006). For this purpose, we have considered a thin FGM plate with uniform distribution (UD) of W^*_{GPL} and carried out a deflection analysis of UD FGM (refer to Figure 7). The earlier existing analytical result for center deflection of the plate calculated from CPT is 2.8524×10^{-5} m (Reddy, 2006) which shows a very close agreement with the current FE results. Due to consideration of the piezoelectric effect, there is a decrement in maximum transverse deflection of the plate compared with non-piezoelectric FGM plate. Having adequate confidence in the finite element model, we present further numerical results based on analytical predictions and finite element analyses.

To check the accuracy of the current quasi-3D sinusoidal shear deformation plate theory with respect to the FE model in case of FGPM LD plates subjected to uniform loading (p_0), the comparative results are plotted in Fig. 8(a). The results are observed to be in excellent agreement, corroborating the validity of the proposed analytical framework further. In the following numerical results, we investigate different critical effects on the electromechanical behaviour of FGPM plates, primarily based on the analytical approach. Figure 8(b) shows the variation of transverse deflection of SSSS FGM and FGPM plates over their lengths considering

linear distribution (LD) of GPLs weight fraction (W^*_{GPL}). A similar trend is observed in UD cases (refer to Figures 7) for transverse deflection, while the LD case shows higher deflection of the plate. A detailed comparison of the results considering LD and UD cases is presented in Figure 9 based on analytical and FE approaches. The results show that the incorporation of piezoelectricity stiffens the FGM plates for both distributions.

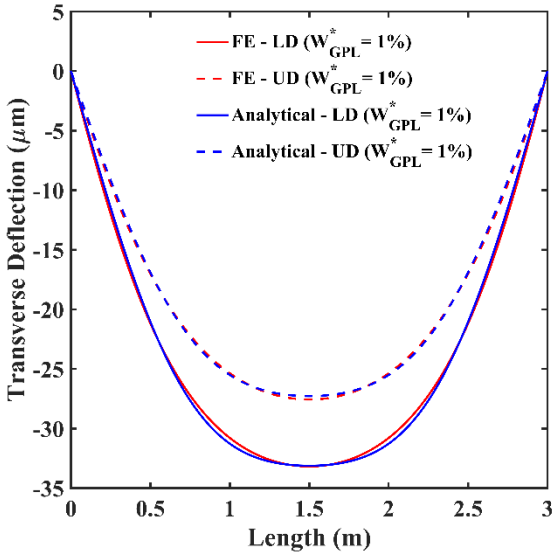

Fig. 9. Effect of distribution of GPLs on the transverse deflection of plates.

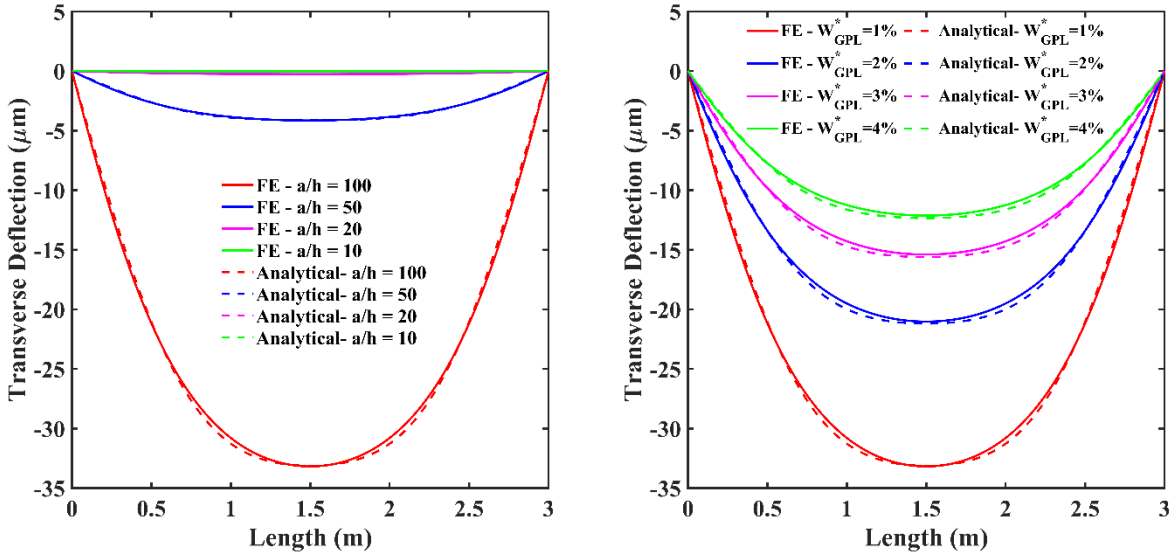

(a) (b)

Fig. 10. Variation of transverse deflection of SSSS FGPM plate along its length (LD case; $V = 0, p_0 = 1$). **(a)** for different aspect ratio ($W^*_{GPL} = 1\%$) **(b)** for different GPL volume fractions ($a/h = 100$).

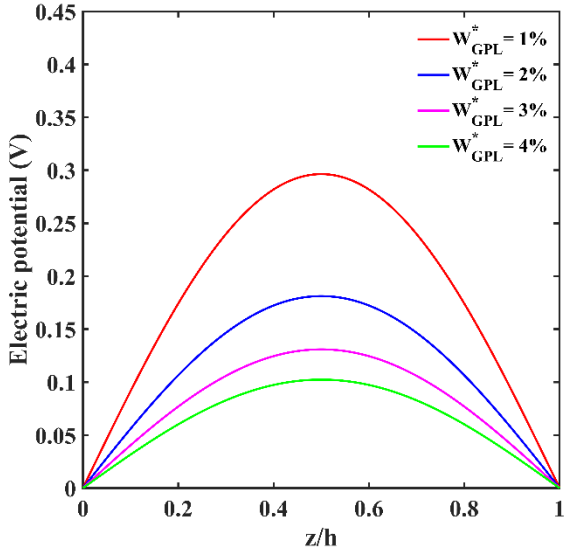

Fig. 11. Variation of electric potential across the thickness of SSSS FGPM plate at its center $(x, y) = \left(\frac{b}{2}, \frac{a}{2}\right)$ (LD case; $a/h = 100, V = 0, p_0 = 1$).

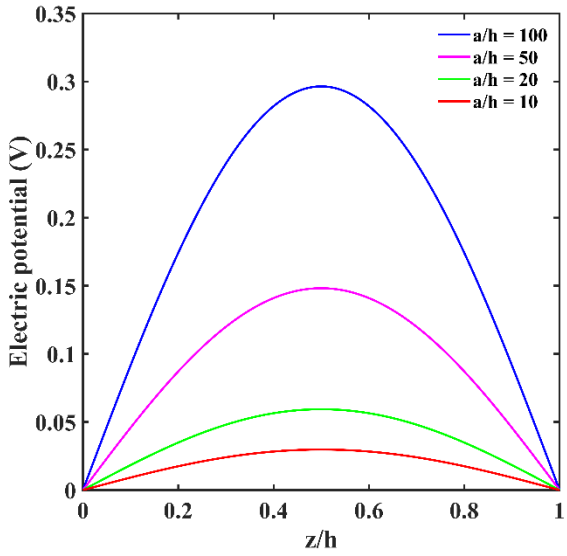

Fig. 12. Variation of electric potential across the thickness of an SSSS FGPM plate at its center $(x, y) = \left(\frac{b}{2}, \frac{a}{2}\right)$ (LD case, $W^*_{GPL} = 1\%, V = 0$).

Figure 10(a) shows the variation of transverse deflection of the SSSS plate over its length by considering different aspect ratios (a/h). For this, we considered $W^*_{GPL} = 1\%$ with LD case while the different aspect ratios are considered as 10, 20, 50 and 100. It is noticed that the transverse deflection increases with increasing aspect ratio. Figure 10(b) shows the variation of transverse deflection of SSSS FGPM plates along their length by considering different W^*_{GPL} with the LD case. From this, it is noticed that the deflection of SSSS

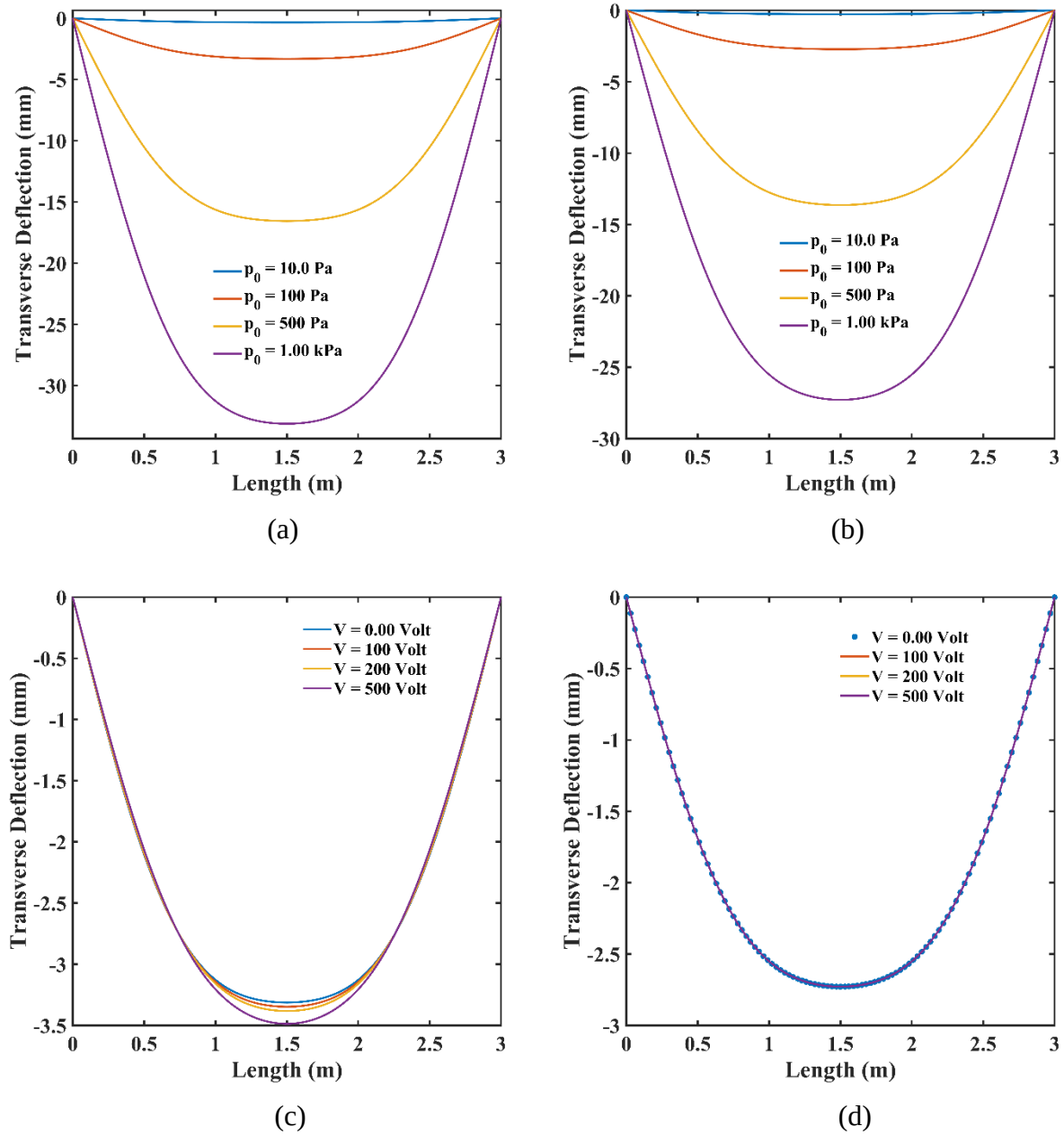

Fig. 13. Variation of transverse deflection of SSSS FGPM plate along the length direction of the plate. (a) LD distribution with a constant voltage of zero throughout the upper surface (along with different values of loads) (b) UD distribution with a constant voltage of zero throughout the upper surface (along with different values of loads) (c) LD distribution when a constant load of 100 Pa is applied on the structure (along with different values of voltage) (d) UD distribution when a constant load of 100 Pa is applied on the structures (along with different values of voltage).

plate is significantly influenced due to the incorporation of nanoparticles such as graphene. The transverse deflection of the plate is reduced due to the addition of a large value of W^*_{GPL}. This effect of different W^*_{GPL} on deflection is also intuitively true as the overall elastic modulus of the model increases if the percentage of GPLs

increases and consequently, it gets stiffer. Further, from Figures 10(a) and 10(b), it is clear that the results obtained from both analytical and FE modelling are observed in excellent agreement.

Figure 11 shows the variation of electric potential generated due to piezoelectricity at the center of SSSS FGPM plate with respect to its thickness by considering different W^*_{GPL}. From this, it can be noted that the electric potential shows the maximum value at the middle of the plate thickness. Similar to transverse deflection, the electric potential decreases due to the addition of different W^*_{GPL}. For $W^*_{GPL} = 1\%$, the electric potential shows larger values compared to the remaining three values of W^*_{GPL}. The electric potential generated in SSSS FGPM plates also depends on the aspect ratios of the plate which are investigated in Figure 12 for aspect ratios of 10, 20, 50 and 100 (considering $W^*_{GPL} = 1\%$). It can be noted that the electric potential increases with respect to the aspect ratio, while the peak voltage appears in the middle layer of the FGPM plate with LD distribution ($W^*_{GPL} = 1\%$ and $a/h = 100$).

The numerical results are presented here (unless otherwise mentioned) considering unit load and zero voltage, which lead to deflections in the micrometer range. The accuracy of the results is ensured through separate finite element simulations. It can be noted that the developed semi-analytical framework is generic enough to analyze larger values of load which would lead to higher deformations. However, to establish the generic nature of the proposed computational framework, we have added two separate studies for single and multi-layered FGPM structures (refer to Figures 13 and 18) where we vary the mechanical load and applied voltage in a reasonable range (complying the small linear strain-displacement assumption). It is observed that the deflections increase significantly with external loads up to the millimeter range. The impact of mechanical load and non-zero voltages on the overall deflection of the plate for both LD and UD FG distributions is shown in Figure 13. Both distributions in Figure 13(a-b) show a direct relationship between transverse deflection (w) and external load (p_0). For instance, in FGPM structure with LD distribution, a maximum deflection of 3.313 mm is observed along the centroidal axis of the plate when a 100 Pa load is applied. In Figure 13(c-d), the piezoelectric voltages are varied for both distributions while maintaining a constant external mechanical stress of 100 Pa. Although the effect of voltage is minimal in UD distribution, the transverse deflection is directly correlated with applied voltages in LD distribution. Overall, the UD distribution in FGPM structures exhibits stiffer behavior than the LD distribution.

4.2 Electromechanical analysis of multilayer FGPM plate

In this Section, we extend the same theoretical approach discussed in Section 2 for presenting numerical results concerning layered composite structures. We have considered a perfectly bonded double-layered FGPM plate ($N_L = 2$) in which GPLs nanofibers are assumed to be randomly oriented in respective matrixes in both the layers with UD/LD configuration. The total thickness is taken as h and it is equally divided in both layers. Distribution of GPLs weight fraction is taken differently in two layers i.e., a top layer having UD distribution

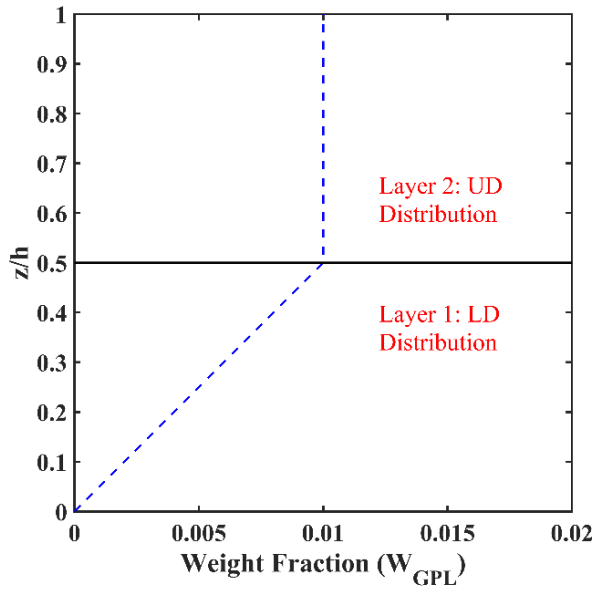

Fig. 14. Distribution of weight fraction of GPLs (W^*_{GPL}) across layered FGPM plate thickness.

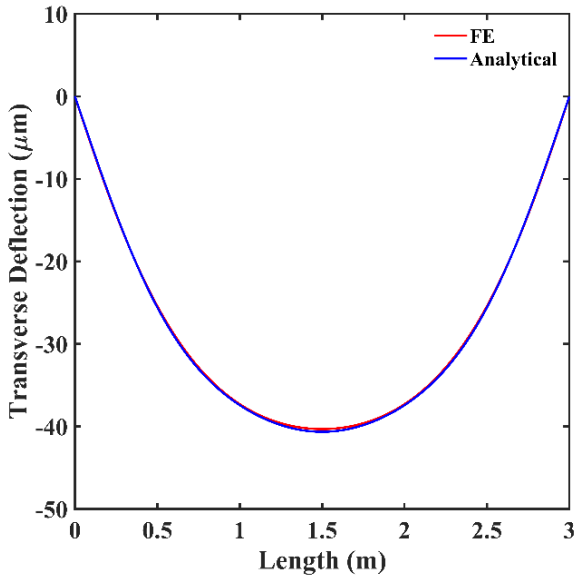

Fig. 15. Variation of transverse deflection of layered FGPM plate along its length ($a/h = 100, W^*_{GPL} = 1\%, p_0 = 1, V = 0$).

and a bottom layer having LD distribution of GPLs. This layer-wise variation of the FGPM plate is depicted in Figure 14. Other boundary conditions remain the same as considered in the single-layer plate. Unit mechanical load and zero external voltage are applied on the outer surface of the plate as before. Both the analytical and FE analyses are performed to check the accuracy of the present theory in predicting the behavior of the layered structure.

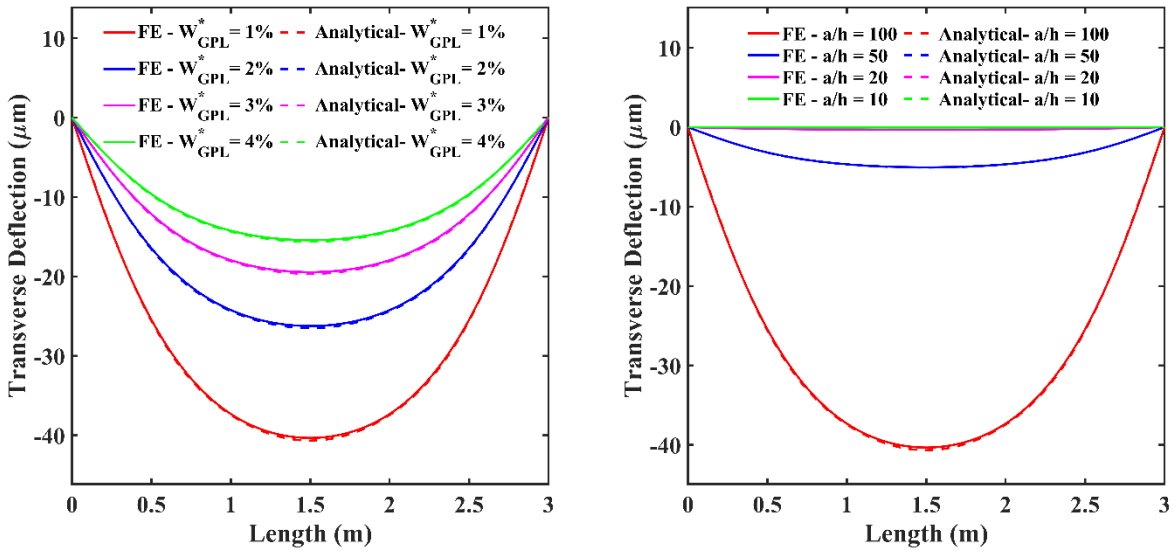

(a) (b)

Fig. 16. (a) Effect of weight fraction of GPLs (W^*_{GPL}) on the transverse deflection of SSSS layered plate $(a/h = 100, p_0 = 1, V = 0)$. **(b)** Effect of aspect ratio (a/h) on the transverse deflection of SSSS layered plate $(W^*_{GPL} = 1\%, p_0 = 1, V = 0)$.

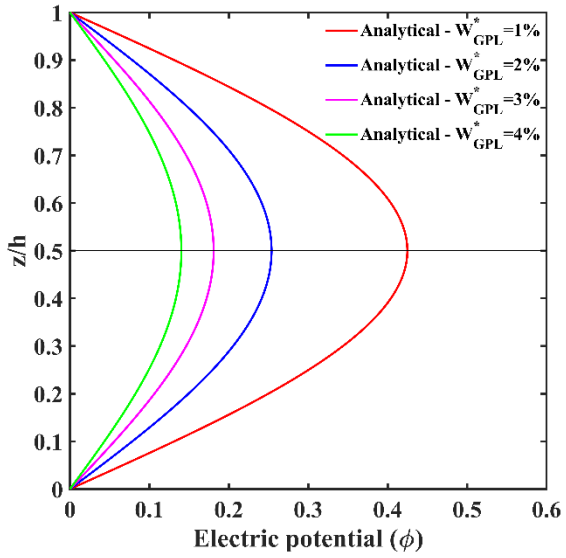

Fig. 17. Variation of electric potential $(\bar{\phi})$ across the thickness of layered FGPM plate at the centre $(x, y) = \left(\frac{b}{2}, \frac{a}{2}\right)$ $(a/h = 100, W^*_{GPL} = 1\%, p_0 = 1, V = 0)$.

Figure 15 shows the variation of transverse deflection of layered FGPM plate along its length. The analytical and FE results for total transverse deflection (w) of the plate under mechanical load $p_0 = 1\ N/m^2$ and electric potential $V = 0$ are compared. From this figure, it is observed that theoretical and FE results are

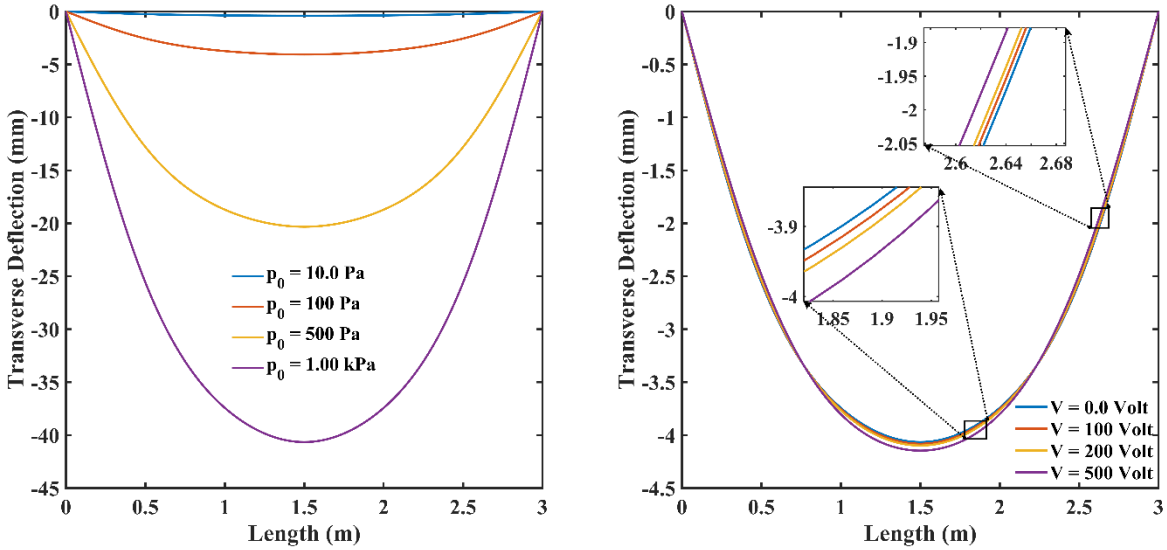

(a) (b)

Fig. 18. Effect of external mechanical load and electrocortical loading on the overall deformation of layered FGPM structures**. (a)** Variation of the plate's deflection along length direction under a constant voltage of zero and different values of mechanical load **(b)** Variation of plate's deflection along length direction under a constant mechanical load of 100 Pa and different values of voltage.

in very good agreement for the multi-layered structures. The maximum deflection is found at the half-length (i.e., 1.5 m) of the plate which is the same in the case of a single-layered plate. From this, we can conclude that number of layers has negligible effects on the overall deflection pattern of the plate if other parameters are kept the same. In figure 15, it is also observed that in the case of multi-layered plates, there is an increment in the magnitude of maximum deflection by 7.94 μm compared to the single-layered plate. A similar trend of the result is observed in existing literature (Lu et al., 2006), which validates our present formulation further.

Subsequently, insightful parametric analysis is performed by varying weight fraction of GPLs (W^*_{GPL}) and plate aspect ratio (a/h), as shown in figures 16(a) and 16(b). The deflection of layered plate decreases as the value of (W^*_{GPL}) and (a/h) increases. It is due to increased stiffness which is discussed in the earlier section. In figure 17, the variation of electric potential along the thickness direction is generated due to the direct piezoelectric effect. It can be observed that the variation is continuous, there is no discontinuity at the interface of the two layers.

Similar to single-layered FGPM distributions (refer to Figure 13), a parametric analysis has been conducted here to check the dependency of external loading parameters on the structure's overall deformation in a multi-layered FGPM system. A significant increase in the maximum transverse deflection in comparison

to its unit-loading state is observed in Figure 18(a) where the deformation increases to the millimeter range with the increase of mechanical loading. Figure 18(b) shows the length-wise change in the plate's deflection with applied voltage. A non-uniform symmetric deformation pattern with respect to plate's centroidal axis can be observed where an increasing trend of deflection with voltage is noticed near the central zone and a reverse decreasing trend of deflection with voltage is obtained near the supporting edge of the plate. Contrary to the uniform trend seen in single layered plates (Figure 13), the double layered (UD/LD) plate here exhibits such non-uniform deformation trend with voltages along its length.

4.3 Time-dependent electromechanical analysis of single and multi-layer viscoelastic FGPM plates

In this section, the time-dependent dynamic behavior of the structure's responses has been investigated by the incorporation of viscoelastic effect. Before obtaining the final results, the effect of viscoelasticity on the effective elastic modulus, $E(z)$ along the thickness has been checked by plotting it in the time domain. As mentioned earlier, this modulus not only depends on time (t) but also the thickness direction (z) since the present structure is depth-wise functionally graded. For each vertical point at a particular section of the plate, we obtain a time-variation curve for the effective elastic modulus. For the sake of brevity, in Table 4, the effect of viscoelasticity on Young's modulus at three locations of the thickness (at $z = -\frac{h}{2}$, $z = 0$ and $z = \frac{h}{2}$) in LD distribution is shown in both the frequency domain and the corresponding transformed time domain. Note that the parameters μ and ϵ in Eq. (29) are crucial for conceptualizing viscoelasticity of the present structure. It is important to keep in mind that the exact values of both parameters (μ and ϵ) in general, depend on different physical experimental outcomes of the relevant viscoelastic system. In particular, they can be obtained from the curve fitting of experimental data concerning creep test of the material. Such experimental implementations were performed in the existing literature (Endo and de Carvalho Pereira, 2017) (Rouleau et al., 2013)(Enelund and Olsson, 1999). As the present study doesn't include any experimental work, we have adopted reasonable parametric values for obtaining the numerical results. Analytically these two parameters, present in complex elasticity modulus ($E_z^*(\omega)$) in the frequency domain, come from the viscoelastic kernel function in the time-domain. This function can be obtained by constructing various equivalent lumped spring-dashpot damping models for viscoelastic material such as Maxwell model, Voigt model, Standard linear model, Generalised Maxwell model and Prony series model. Whereas, in the frequency or Laplace domain, various existing viscoelastic models complying Kramers-Kronig relations can be used to derive $E_z^*(\omega)$ such as Biot model, Gaussian model, Fractional derivative, Half cosine model etc. Among them, the Biot's standard classical model of viscoelasticity (Biot, 1955)(Biot, 1954) has been chosen here by which complex elasticity modulus ($E_z^*(\omega)$) can be obtained without any significant accuracy loss. To examine the effect of the two parameters on overall strength of viscoelastic model, a parametric study (refer to Figure 19(a-d)) is presented. First, we have investigated the influence of these two parameters on the present viscoelastic system and afterwards, a suitable

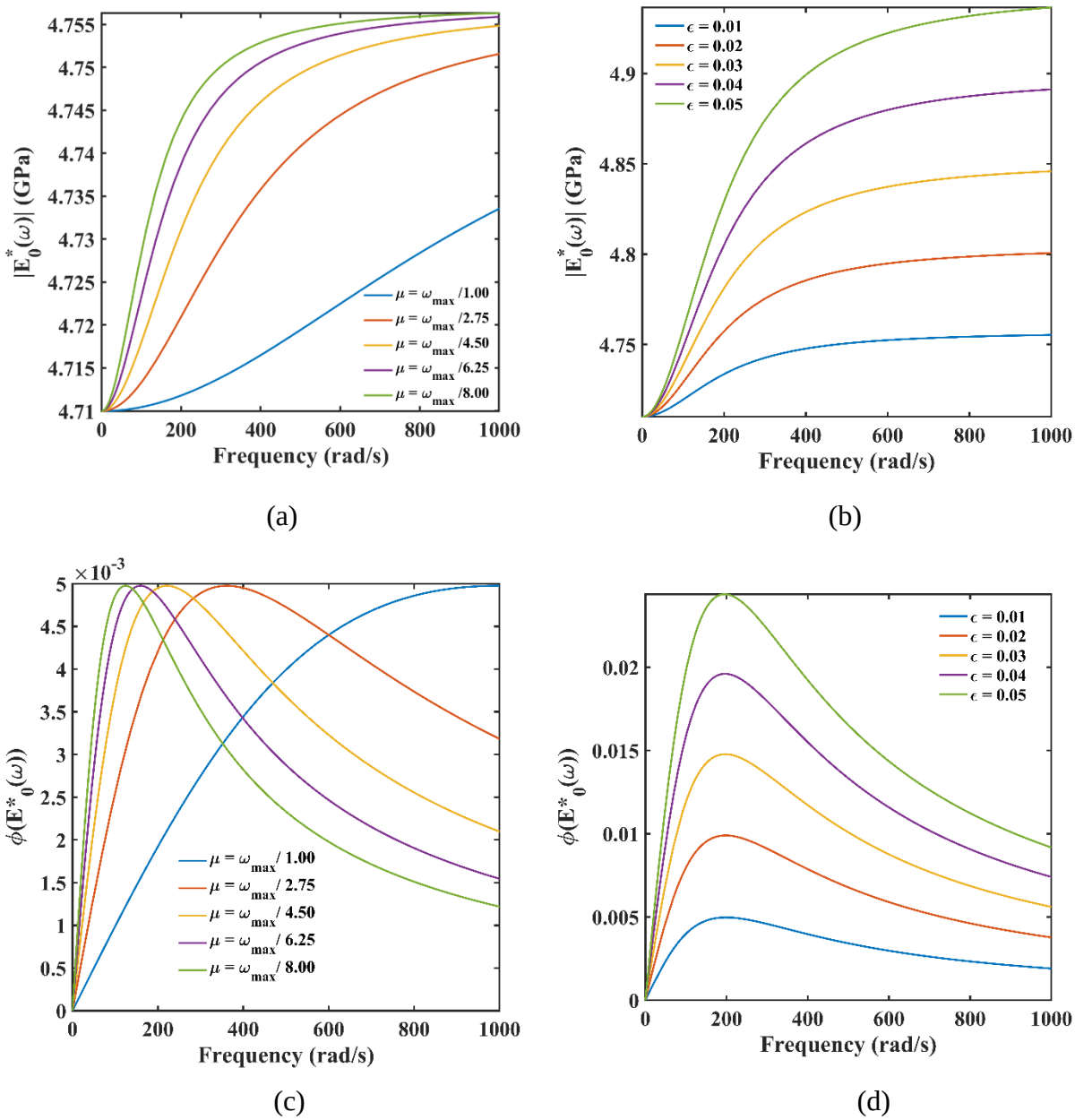

Fig. 19. (a) Effect of the parameter μ of the amplitude of mid-plane-Young-modulus in the frequency domain at constant $\epsilon = 0.01$. **(b)** Effect of the parameter ϵ of the amplitude of mid-plane-Young-modulus in the frequency domain at constant $\mu = \frac{(\omega_{max})}{5}$. **(c)** Effect of the parameter μ of the magnitude of viscoelastic phase angle at mid-plane in the frequency domain at constant $\epsilon = 0.01$. **(d)** Effect of the parameter μ of the magnitude of viscoelastic phase angle at mid-plane in the frequency domain at constant $\mu = \frac{(\omega_{max})}{5}$.

combination of their values are chosen to produce numerical results in succeeding sections. It can be noted that the temporal framework presented here is generic and any suitable value of μ and ϵ, obtained based on experimental investigations, can be used for exploration of the viscoelastic behaviour. In Figure 19(a-d), the

amplitude of Young modulus at mid-plane and its associated phase angle are varied in a reasonable frequency range for different values of μ and ϵ. It can be seen in Figure 19(a-b) that the amplitude increases as the values of μ and ϵ reduce and increase respectively. They all show converging patterns in the values after certain frequencies. This can be explained with the help of Figure 19(c-d). Figure 19(c) depicts the variation of phase angle in frequency domain for different μ at a constant $\epsilon = 0.01$, whereas the same is plotted in Figure 19(d) for different ϵ taking μ as constant i.e. $\mu = \frac{(\omega_{max})}{5}$ (where ω_{max} is the maximum magnitude of considered frequency spectrum). Existence of critical frequencies can be observed, wherein the physical significance of such critical frequency can be explained in the light of spring-dashpot lumped model of viscoelasticity. At very low and high frequencies, the model behaves as pure elastic, whilst in the vicinity of the critical frequency, the viscous effects become maximum. That is why in Figure 19(a-b), at very low frequency, amplitude of Young modulus takes a constant non-zero value and after a certain frequency, it again converges to a constant non-zero value. From Figure 19(c-d), it can be concluded that the parameter μ controls the critical frequency whereas the parameter ϵ shows its influence on magnitude of phase angle of the present viscoelastic model.

After the afore-explained parametric study investigating the influence of viscoelastic parameters, we can now proceed for obtaining numerical results in the current context by taking a combination of these two parameters μ and ϵ. In the frequency domain, the variation of the dynamic modulus and its phase is obtained by taking the parameters as $\mu = \frac{(\omega_{max})}{1.4}$ and $\epsilon = 0.01$ for the present paper. Except for Young's moduli, Poisson's ratio and other piezoelectric properties are considered to have a negligible effect of viscoelasticity based on published literature (Salehi and Aghaei, 2005, Salehi and Safi-djahanshahi, 2010, Barrett and Gotts, 2004). It has also been verified in MATLAB that the values of elastic modulus in all three cases (refer to Table 4) at low frequency ($\omega \sim 0$) are the same as the non-viscous elastic modulus mentioned in the prior sections. Such observations are in coherence with the existing literature (Mukhopadhyay et al., 2019, Malekmohammadi et al., 2014). In Table 4, the variation of phase angle in all three locations has also been plotted and it is observed that all are the same and achieve their peak value at a certain critical frequency. So, the phase angle variation is independent of thickness direction, though the amplitude of elastic moduli keeps changing with the thickness direction. The phase angle decreases on both sides of the frequency spectrum i.e. at the lowest and highest frequency of the plot. At low frequencies, the present viscoelastic plate will behave more like a normal elastic plate. After applying the inverse Fourier algorithm, the time domain plots are obtained along the thickness. As time increases, elastic moduli keep decreasing and after a certain time, it gets converged at their non-viscous elastic moduli value ($\lim_{t\to\infty} E_z(t, z_0) = E(z_0)$). Such a trend has also been observed in the existing literature (García-Barruetabeña et al., 2013).

Table 4: Variation of the effective Young Modulus in frequency and corresponding time domain at three locations of the thickness (LD distribution).

Position	Frequency Domain	Time Domain
$-h/2$	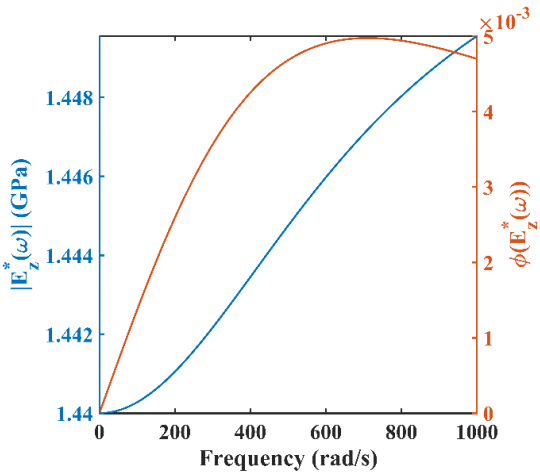	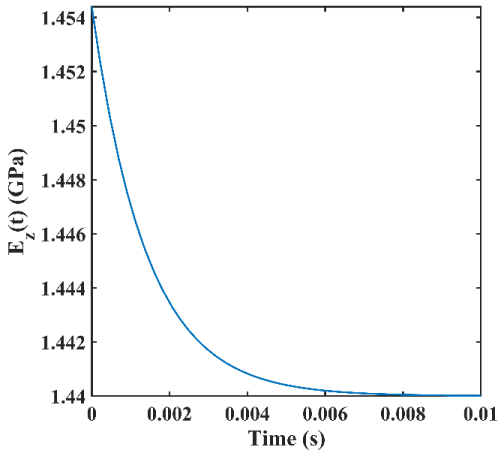
0	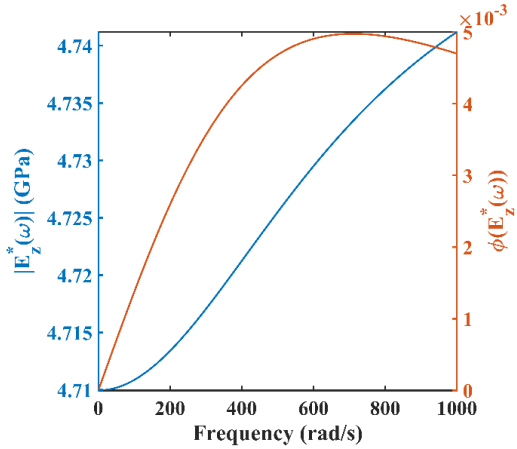	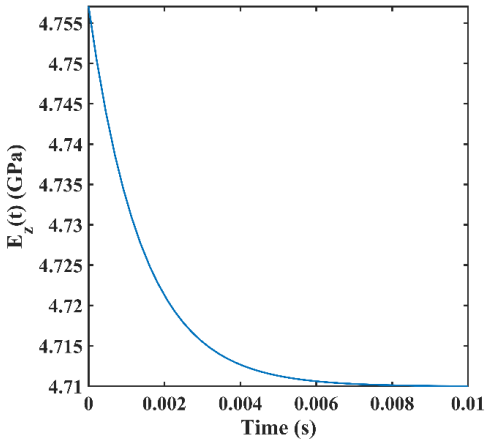
$h/2$	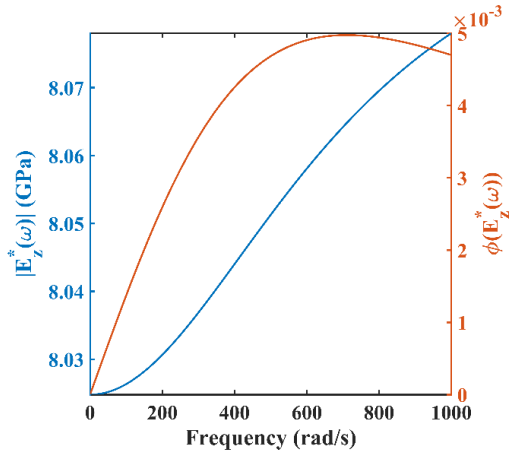	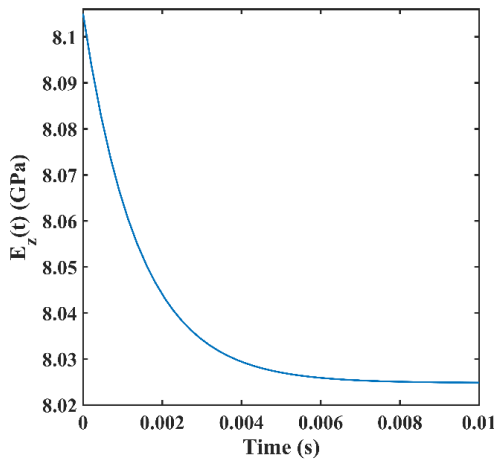

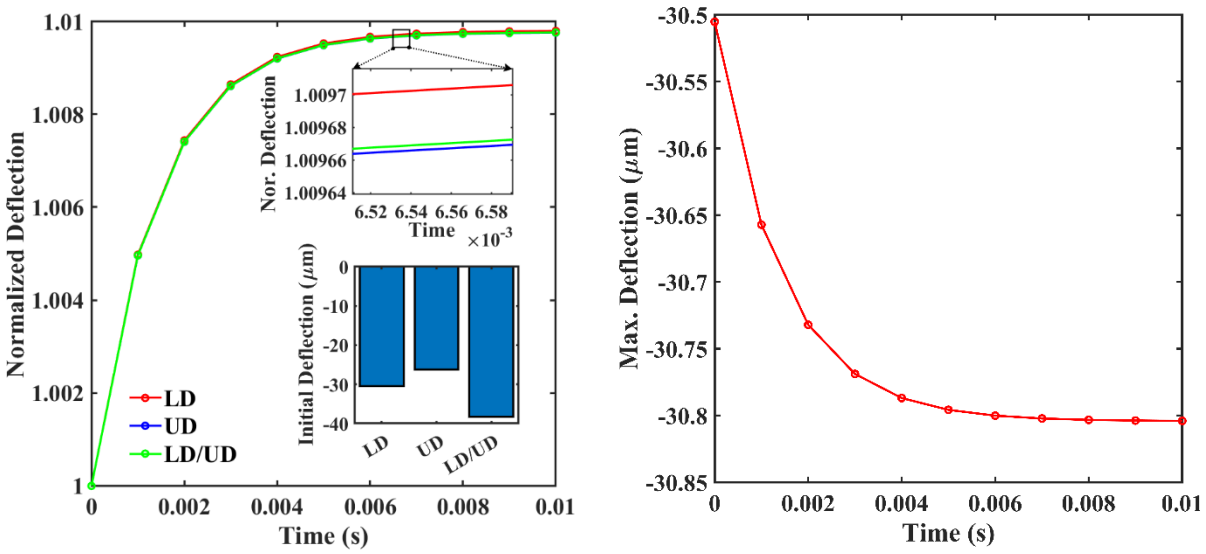

(a) (b)

Fig. 20. Time-dependent variation of plate's deflection **(a)** in UD, LD and LD/UD cases in terms of normalized form **(b)** in LD case in terms of absolute form. The normalization is carried out here with respect to the deflection value at initial time step (t = 0), as shown in the inset. In the axis titles of the inset figures, Nor. representes Normalized.

The obtained depth-wise varying elastic moduli in the time domain are now embedded within the analytic model to obtain the time-dependent responses of the viscoelastic FGPM plate, subjected to the aforementioned boundary conditions ($V = 0, p_0 = 1$, SSSS). Figure 20(a) depicts the effect of viscoelasticity on the plate's deflection under the unit uniform static transverse load. Here the normalized maximum deflections ($\bar{w}_{max}$) along the centroidal axis of the plate are plotted for the single-layered (LD and UD distribution) and multi-layered (LD/UD) FGPM plate. In terms of final (saturated) normalized deflection, it is observed that the multi-layered (LD/UD) plate is between the rest two distributions where LD is having the highest value of the same. It indicates the fact that the increment of the plate's deflection with time is highest in LD distribution, while LD/UD plate is in between the two. Although, in terms of absolute deflection, the deflection in LD/UD plate at its saturation stage is higher than the rest two. In each case, this maximum deflection converges at a certain deflection which is almost the same as that of pure elastic case. For instance, in LD distribution, the FGPM plate starts bending with a maximum deflection of 30.51 μm under the constant load of 1 N/m^2 and after 0.01 sec, its deflection increases to a deflection of around 30.8 μm. The bar charts in Figures 20-22 are showing the initial deflections ($t = 0$) in μm. Due to the incorporation of viscoelasticity, we can see a time lag in achieving its prior elastic deflection. A similar trend is observed in other distributions as well. But the rate of change in the deflection in three distributions is found to be different depending on the

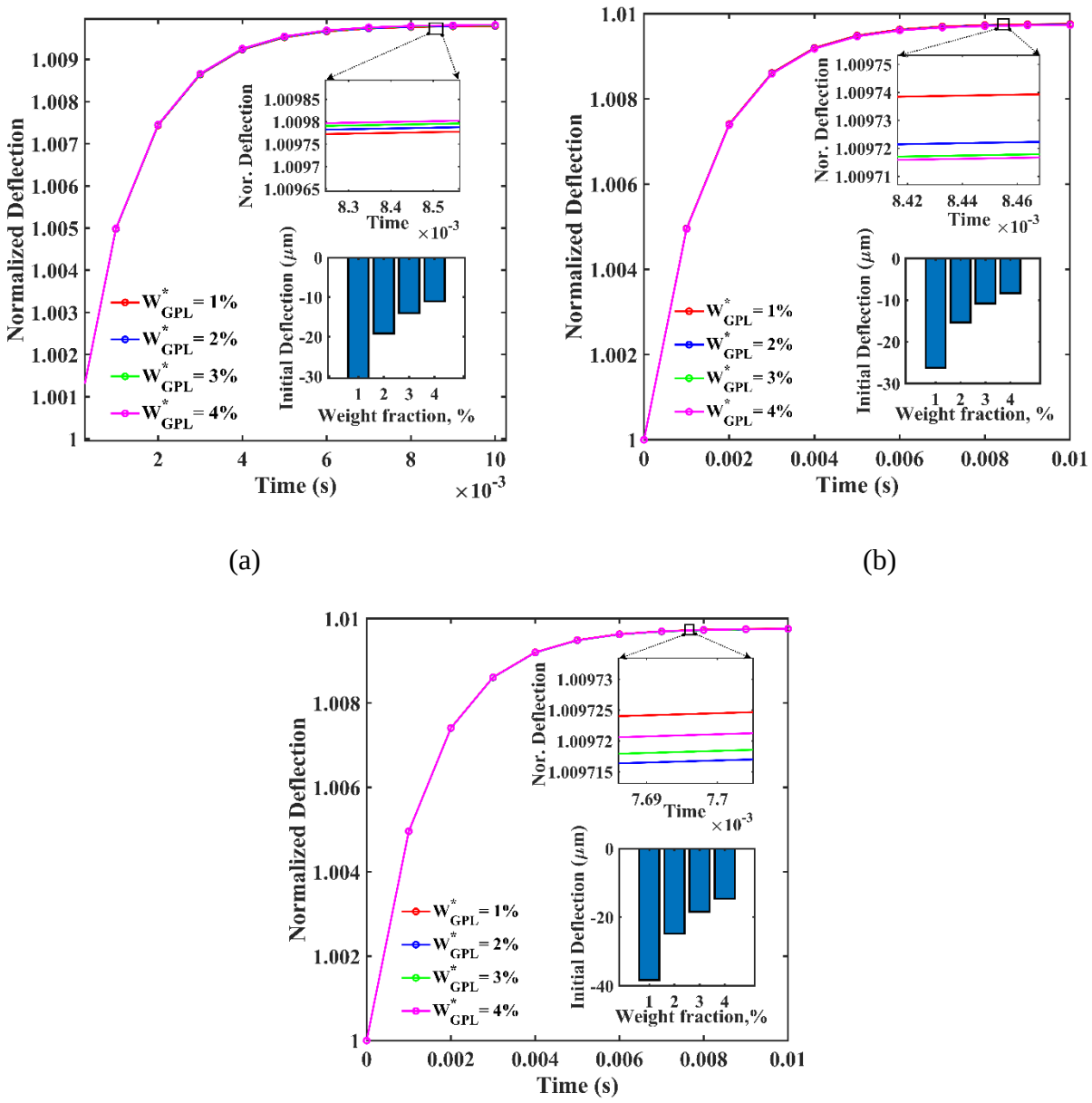

Fig. 21. Effect of viscoelasticity on the maximum transverse deflection of the FGPM plate with four different volume fractions of GPL **(a)** LD **(b)** UD **(c)** LD/UD. The normalization is carried out here with respect to the deflection value at initial time step (t = 0), as shown in the inset. In the axis titles of the inset figures, Nor. representes Normalized.

distribution (Multi-layered FGPM > Single-layered LD FGPM > Single-layered UD FGPM). For the sake of clarity, the time variation (discussed in Figure 20(a)) in terms of absolute deflection for only LD distribution is shown in Figure 20(b) (similar plots can be readily obtained for the other distributions). The trends are in good coherence with the existing literature on non-FGPM viscoelastic plate structures (Jafari and Azhari, 2021, Salehi and Aghaei, 2005, Wenzel et al., 2009).

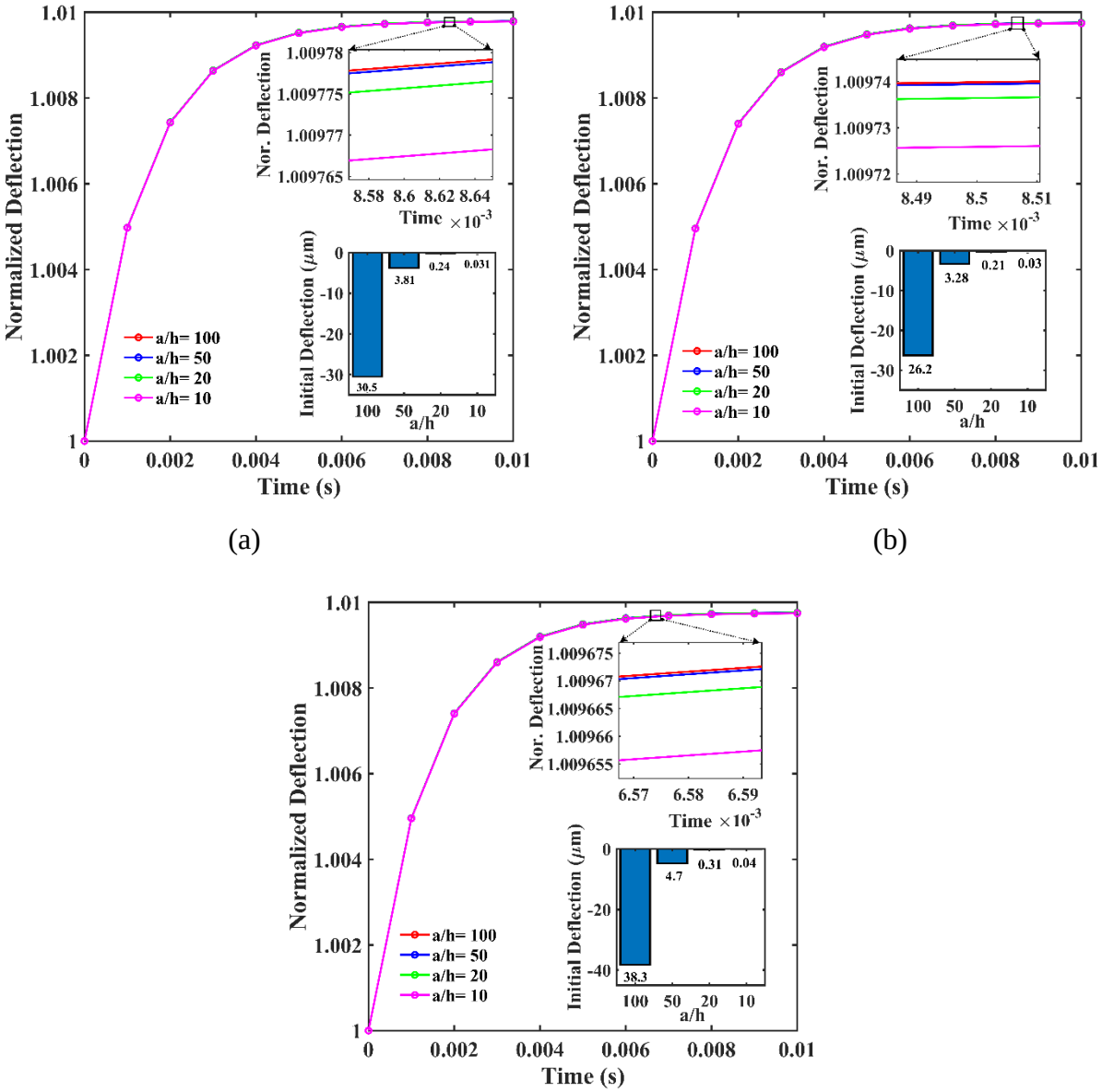

Fig. 22. Effect of viscoelasticity on the maximum transverse deflection of the FGPM plate with four different plate aspect ratios ($b = 3, \mathrm{V} = 0, \mathrm{p}_0 = 1$) **(a)** LD **(b)** UD **(c)** LD/UD. The normalization is carried out here with respect to the deflection value at initial time step (t = 0), as shown in the inset. In the axis titles of the inset figures, Nor. representes Normalized.

Figure 21 shows the viscoelastic effect on the plate's central deflection at four different volume fractions i.e. $W^*_{GPL} = 1\%, 2\%, 3\%, 4\%$ of GPLs in the PVDF matrix. With the increase of volume fraction, the plate's elastic deflection at $t = 0$ and the steady state ($t = \infty$) both decrease. Moreover, the rates of deformation are found to be decreased with the increase of GPL's volume fraction. For the increment of deflection in each FGM distribution, all three show different trends with respect to volume fractions. For instance, in LD plate, the increment goes up as the volume fraction increases, whereas in UD case, the opposite

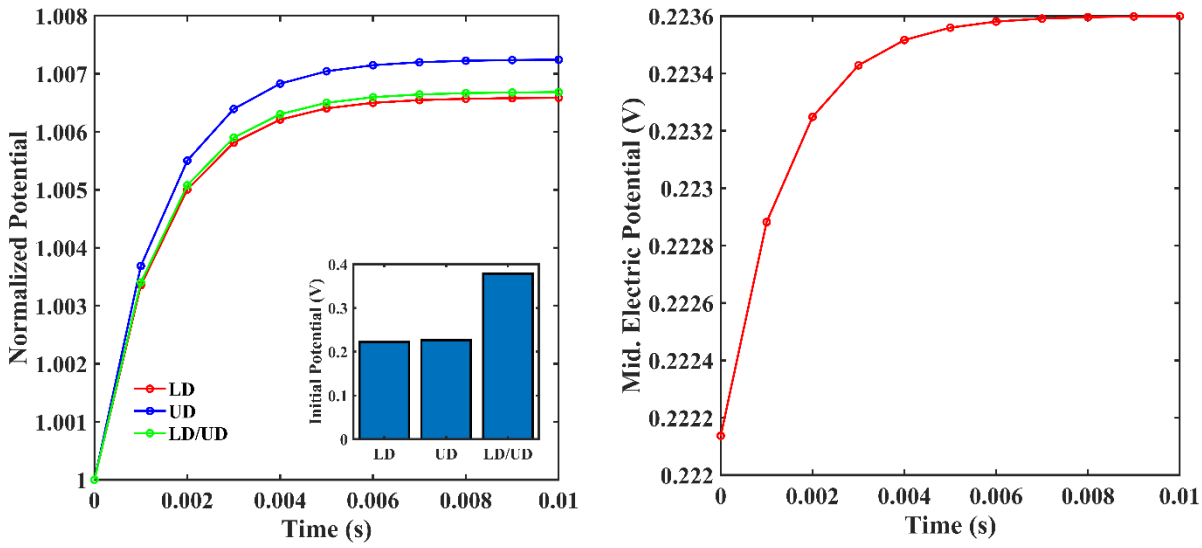

(a) **(b)**

Fig. 23. Time-dependent variation of plate's mid-line electric potential ($W^*_{GPL} = 1\%$ and $a/h = 100$) **(a)** in UD, LD and LD/UD cases in terms of normalized form **(b)** in LD case in terms of absolute form. The normalization is carried out here with respect to the potential value at initial time step (t = 0), as shown in the inset.

trend is observed. A little exception is identified in LD/UD plate as here the normalized deflection rises with volume fractions except the one with 1% volume fraction whose increment is higher than rest three in Figure 21(c).

In Figure 22, the aspect ratio of FGPM plates is varied over a reasonable range to observe the effect of viscoelasticity on the plate's deformation. Contrary to the trend observed in the aforementioned volume fractions' cases, both the deflections (at $t = 0$ and $t = \infty$) are in direct relation with the plate's aspect ratio. The rate of deformation here is found to have a rapid increment with the increase of aspect ratio. Furthermore, the increment in deflection with respect to its initial value ($t = 0$) is observed to have a direct relation with plate's aspect ratio in all three distributions. In general, the numerical study considering viscoelastic behaviour, besides giving a more realistic analysis, demonstrates a potential programmable time-dependent structural behaviour (including temporal programming in smart stuctures and metamaterials (Sinha and Mukhopadhyay, 2023)), which could be crucial for analysing and designing the mechanical behaviour of a wide range of polymer composites accurately.

The time-dependent generation of electric potential in the present FGPM viscoelastic system is shown in Figure 23(a) where all three FGM distributions show rapid growth in their values with time. These depicted

potentials are extracted along the centroidal axis of the plate and with the consideration of GPL percentage of 1% and plate's length-to-thickness ratio of 100. Though the double-layered plate gives a relatively higher voltage (~70% higher) than the rest of the distributions after getting saturated, the increment of it with respect to initial electric potential over time is in between the other two distributions where the uniformly distributed (UD) FGPM plate shows the highest increment. Figure 23(b) shows the same time-variation of electric potential in LD distribution but in its absolute form, leading to the same conclusion (similar plots can be readily obtained for the other distributions). Essentially, the numerical results concerning electric potential for time-dependent viscoelastic analysis shows that it is possible to harness more accumulated power with increasing time.

5. Prospective engineering applications

Functionally graded piezoelectric material (FGPM) viscoelastic composite structures combine the properties of piezoelectric materials and viscoelastic composites to create a class of materials with unique prospective engineering applications. Such an analysis following efficient semi-analytical framework is presented for the first time in this manuscript. We have discussed here a few critical real-life engineering applications associated with FGPM viscoelastic composite structures.

- *Shape Morphing Structures:* FGPM viscoelastic composite materials can be engineered to change their shape in response to electrical stimuli. These materials are used to create adaptive structures and morphing surfaces in aerospace applications, where shape changes can improve aerodynamic performance. Similar applications can be found in various other mechanical systems. The interesting notion here is the capability of temporal programming as discussed in the manuscript.
- *Energy Absorption:* FGPM viscoelastic composites can be employed in impact-absorbing structures, such as helmet liners and automotive crash pads. The combination of viscoelastic damping and piezoelectric energy conversion helps dissipate energy during impact events, reducing the risk of injury and damage.
- *Smart Materials and Structures:* FGPM viscoelastic composites can be utilized in the development of smart materials and structures. By exploiting their piezoelectric properties, these materials can sense changes in the operating environment and respond accordingly, enabling applications like active vibration control, actuators, shape adaptation, programmable mechanical properties etc. In microelectromechanical systems (MEMS), FGPM viscoelastic composites can be utilized in the fabrication of tiny sensors, actuators, and resonators for applications in various mechanical, aerospace, consumer electronics, and medical sectors.

- *Structural Health Monitoring:* FGPM viscoelastic composite structures can be used for structural health monitoring (SHM) purposes. They can be embedded with sensors that utilize the piezoelectric effect to detect changes in the systems's properties and identify structural damage or defects in real time.
- *Soft Robotics:* FGPM viscoelastic composites can be integrated into soft robotic systems to create deformable structures with piezoelectric functionality. These materials would enable more flexible and adaptable robots for delicate tasks and human-robot interaction.
- *Vibration Damping and Control:* FGPM viscoelastic composite structures can be employed in the aerospace, automotive, and civil engineering industries for vibration damping and control. These materials can be designed to have specific damping properties, reducing vibrations and minimizing resonance effects in structures like aircraft wings, car panels, and buildings.

6. Concluding remarks

In this article, we have investigated the time-dependent viscoelastic electromechanical behaviour of single and multi-layered piezoelectric functionally graded graphene-reinforced composite (FG-GRC) plates (called FGM and FGPM plates). Higher-order shear deformation theory (HSDT) with quasi-3D plate formulation that incorporates sinusoidal shape function and linear piezoelectricity are implemented along with the Biot model of viscoelasticity in the framework of the inverse Fourier algorithm. The principle of virtual work is adopted to derive the governing equations and boundary constraints for analytical solutions based on Navier's method. Further, finite element models are developed to confirm the accuracy and validity of the analytical results. The electromechanical behaviour includes the static and electric response of FG-GRC viscoelastic plates which are predicted considering transverse mechanical and external electrical loading under simply supported (SSSS) conditions. Following major inferences are drawn from the numerical results:

- The transverse deflection of FGM and FGPM plates are significantly affected due to consideration of piezoelectricity, weight fraction of GPLs (W^*_{GPL}) and different distribution patterns (such as linear and uniform distribution) of GPLs along the thickness. It increases with respect to aspect ratio (a/h) while reduces for a larger value of W^*_{GPL}.
- The electric potential shows significant enrichment with higher values of a/h ratio, while it shows a decrement with respect to the addition of W^*_{GPL}.
- A rapid decrement in the elastic properties of FG-GRC plates can be observed with time due to the consideration of the viscoelastic effect.
- The numerical results concerning electric potential for time-dependent viscoelastic analysis establishes that it is possible to harness more accumulated power with increasing time before eventually reaching the steady state condition. With regard to the aspect ratio of the plate, weight fractions of the GPL and

the distribution patterns, the steady-state values follow a similar general trend as the non-viscoelastic scenario.

- All three distributions exhibit a rapid increment in transverse deformation and electric potential with time, although the rates at which this increment occurs vary depending on the distribution of the material properties (Multi-layered FGPM > Single-layered LD FGPM > Single-layered UD FGPM).

In summary, the current semi-analytical study demonstrates a potential time-dependent electromechanical behaviour based on practically relevant viscoelastic modelling coupled with through-thickness gradation, which could be crucial for analysing the structural behaviour of a wide range of 'smart' plate-like structures accurately and prospective temporal programming for a range of engineering applications across the length scales. The present analytical solution approach can also be extended to obtain the viscoelastic electromechanical responses of functionally graded smart shells and other complicated structural assemblies. The combination of piezoelectricity and viscoelasticity in FGPM viscoelastic composite structures opens up a wide range of engineering possibilities, from energy harvesting, vibration control, shape-morphing to advanced robotics and smart structures. Ongoing research in this field continues to explore new applications and optimize the performance of these materials for real-world scenarios.

Acknowledgments

TM and SN acknowledge the initiation grant received from the University of Southampton.

Conflict of Interest

The authors declare no conflict of interest.

ORCID ID

Soumyadeep Mondal : https://orcid.org/0000-0002-3368-7828

Kishor Shingare https://orcid.org/0000-0002-8255-9849

Tanmoy Mukhopadhyay https://orcid.org/ 0000-0002-0778-6515

Susmita Naskar https://orcid.org/0000-0003-3294-8333

References

Aboudi, J., Cederbaum, G., 1989. Analysis of viscoelastic laminated composite plates. Compos. Struct. 12, 243–256. https://doi.org/10.1016/0263-8223(89)90074-3

Amoushahi, H., Azhari, M., 2014. Static and instability analysis of moderately thick viscoelastic plates using a fully discretized nonlinear finite strip formulation. Compos. Part B Eng. 56, 222–231. https://doi.org/10.1016/j.compositesb.2013.08.055

Assadi, A., Farshi, B., 2011. Stability analysis of graphene based laminated composite sheets under non-

uniform inplane loading by nonlocal elasticity. Appl. Math. Model. 35, 4541–4549. https://doi.org/10.1016/j.apm.2011.03.020

Barati, M.R., Zenkour, A.M., 2019. Thermal post-buckling analysis of closed circuit flexoelectric nanobeams with surface effects and geometrical imperfection. Mech. Adv. Mater. Struct. 26, 1482–1490. https://doi.org/10.1080/15376494.2018.1432821

Barrett, K.E., Gotts, A.C., 2004. FEM for one- and two-dimensional viscoelastic materials with spherical and rotating domains using FFT. Comput. Struct. 82, 181–192. https://doi.org/10.1016/j.compstruc.2003.10.007

Beeby, S.P., Tudor, M.J., White, N.M., 2006. Energy harvesting vibration sources for microsystems applications. Meas. Sci. Technol. 17. https://doi.org/10.1088/0957-0233/17/12/R01

Behjat, B., Salehi, M., Armin, A., Sadighi, M., Abbasi, M., 2011. Static and dynamic analysis of functionally graded piezoelectric plates under mechanical and electrical loading. Sci. Iran. 18, 986–994. https://doi.org/10.1016/j.scient.2011.07.009

Biot, M.A., 1955. Variational principles in irreversible thermodynamics with application to viscoelasticity. Phys. Rev. 97, 1463–1469. https://doi.org/10.1103/PhysRev.97.1463

Biot, M.A., 1954. Theory of stress-strain relations in anisotropic viscoelasticity and relaxation phenomena. J. Appl. Phys. 25, 1385–1391. https://doi.org/10.1063/1.1721573

Das, S., Sarangi, S.K., 2016. Static Analysis of Functionally Graded Composite Beams, in: IOP Conference Series: Materials Science and Engineering. https://doi.org/10.1088/1757-899X/149/1/012138

Endo, V.T., de Carvalho Pereira, J.C., 2017. Linear orthotropic viscoelasticity model for fiber reinforced thermoplastic material based on Prony series. Mech. Time-Dependent Mater. 21, 199–221. https://doi.org/10.1007/s11043-016-9326-8

Enelund, M., Olsson, P., 1999. Damping described by fading memory - Analysis and application to fractional derivative models. Int. J. Solids Struct. 36, 939–970. https://doi.org/10.1016/S0020-7683(97)00339-9

FUCHIYAMA, T., 1993. Analysis of thermal stress and stress intensity factor of functionally gradient materials. Ceram. Trans. Funct. Gradient Mater. 34, 425–430.

Fukui, Y., Yamanaka, N., 1992. Elastic analysis for thick-walled tubes of functionally graded material subjected to internal pressure. JSME Int. Journal, Ser. 1 Solid Mech. Strength Mater. 35, 379–385. https://doi.org/10.1299/jsmea1988.35.4_379

Fukui, Y., Yamanaka, N., Wakashima, K., 1993. Stresses and strains in a thick-walled tube for functionally graded material under uniform thermal loading. JSME Int. Journal, Ser. A Mech. Mater. Eng. 36, 156–162. https://doi.org/10.1299/jsmea1993.36.2_156

García-Barruetabeña, J., Cortés, F., Abete, J.M., Fernández, P., Lamela, M.J., Fernández-Canteli, A., 2013. Relaxation modulus - Complex modulus interconversion for linear viscoelastic materials. Mech. Time-Dependent Mater. 17, 465–479. https://doi.org/10.1007/s11043-012-9197-6

Gholami, R., Ansari, R., 2018. Nonlinear harmonically excited vibration of third-order shear deformable functionally graded graphene platelet-reinforced composite rectangular plates. Eng. Struct. 156, 197–209. https://doi.org/10.1016/j.engstruct.2017.11.019

Gholami, R., Ansari, R., 2017. Large deflection geometrically nonlinear analysis of functionally graded multilayer graphene platelet-reinforced polymer composite rectangular plates. Compos. Struct. 180, 760–

771. https://doi.org/10.1016/j.compstruct.2017.08.053

Guo, H., Cao, S., Yang, T., Chen, Y., 2018. Vibration of laminated composite quadrilateral plates reinforced with graphene nanoplatelets using the element-free IMLS-Ritz method. Int. J. Mech. Sci. 142–143, 610–621. https://doi.org/10.1016/j.ijmecsci.2018.05.029

Halpin, J.C., Karoos, J.L., 1978. Strength of discontinuous reinforced composites: I. Fiber reinforced composites. Polym. Eng. Sci. 18, 496–504. https://doi.org/10.1002/pen.760180612

Jafari, N., Azhari, M., 2021. Time-dependent static analysis of viscoelastic Mindlin plates by defining a time function. Mech. Time-Dependent Mater. 25, 231–248. https://doi.org/10.1007/s11043-019-09437-w

Karsh, P.K., Mukhopadhyay, T., Chakraborty, S., Naskar, S., Dey, S., 2019. A hybrid stochastic sensitivity analysis for low-frequency vibration and low-velocity impact of functionally graded plates. Compos. Part B Eng. 176. https://doi.org/10.1016/j.compositesb.2019.107221

Karsh, P.K., Mukhopadhyay, T., Dey, S., 2018. Stochastic dynamic analysis of twisted functionally graded plates. Compos. Part B Eng. 147, 259–278. https://doi.org/10.1016/j.compositesb.2018.03.043

Kuai, W.J., Zhao, M.L., Wang, C.L., Wang, L.H., Wang, J., Gai, Z.G., Zhang, J.L., Yin, N., 2013. Effect of composition on the structure and piezoelectricity of Na 0.5Bi4.5Ti4O15-based flexoelectric-type polar ceramics. J. Alloys Compd. 559, 76–80. https://doi.org/10.1016/j.jallcom.2013.01.077

Levy, M., 1877. Mémoire sur la théorie des plaques élastiques planes. J. Math. Pures Appl. 3, 219–306.

Li, C., Han, Q., Wang, Z., Wu, X., 2020. Analysis of wave propagation in functionally graded piezoelectric composite plates reinforced with graphene platelets. Appl. Math. Model. 81, 487–505. https://doi.org/10.1016/j.apm.2020.01.016

Lu, P., Lee, H.P., Lu, C., 2006. Exact solutions for simply supported functionally graded piezoelectric laminates by Stroh-like formalism. Compos. Struct. 72, 352–363. https://doi.org/10.1016/j.compstruct.2005.01.012

Malekmohammadi, S., Tressou, B., Nadot-Martin, C., Ellyin, F., Vaziri, R., 2014. Analytical micromechanics equations for elastic and viscoelastic properties of strand-based composites. J. Compos. Mater. 48, 1857–1874. https://doi.org/10.1177/0021998313490977

Malekzadeh, P., Setoodeh, A.R., Shojaee, M., 2018. Vibration of FG-GPLs eccentric annular plates embedded in piezoelectric layers using a transformed differential quadrature method. Comput. Methods Appl. Mech. Eng. 340, 451–479. https://doi.org/10.1016/j.cma.2018.06.006

Maranganti, R., Sharma, N.D., Sharma, P., 2006. Electromechanical coupling in nonpiezoelectric materials due to nanoscale nonlocal size effects: Green's function solutions and embedded inclusions. Phys. Rev. B - Condens. Matter Mater. Phys. 74. https://doi.org/10.1103/PhysRevB.74.014110

Mondal, S., Agnihotri, S.K., Faye, A., 2022. Theoretical solution for thermo-mechanical crack-tip stress field for transversely graded materials. J. Therm. Stress. 45, 101–116. https://doi.org/10.1080/01495739.2022.2030837

Mukhopadhyay, T., Adhikari, S., Batou, A., 2019. Frequency domain homogenization for the viscoelastic properties of spatially correlated quasi-periodic lattices. Int. J. Mech. Sci. 150, 784–806. https://doi.org/10.1016/j.ijmecsci.2017.09.004

Mukhopadhyay, T., Naskar, S., Chakraborty, S., Karsh, P.K., Choudhury, R., Dey, S., 2021. Stochastic Oblique Impact on Composite Laminates: A Concise Review and Characterization of the Essence of Hybrid

Machine Learning Algorithms, Archives of Computational Methods in Engineering. https://doi.org/10.1007/s11831-020-09438-w

Mun, S., Chehab, G.R., Kim, Y.R., 2007. Determination of Time-domain Viscoelastic Functions using Optimized Interconversion Techniques. Road Mater. Pavement Des. 8, 351–365. https://doi.org/10.1080/14680629.2007.9690078

Naskar, S., Shingare, K.B., Mondal, S., Mukhopadhyay, T., 2022. Flexoelectricity and surface effects on coupled electromechanical responses of graphene reinforced functionally graded nanocomposites: A unified size-dependent semi-analytical framework. Mech. Syst. Signal Process. 169. https://doi.org/10.1016/j.ymssp.2021.108757

Natarajan, S., Ferreira, A.J.M., Bordas, S., Carrera, E., Cinefra, M., Zenkour, A.M., 2014. Analysis of functionally graded material plates using triangular elements with cell-based smoothed discrete shear gap method. Math. Probl. Eng. 2014. https://doi.org/10.1155/2014/247932

Nomura, S., Sheahen, D.M., 1997. Micromechanical approach to the thermomechanical analysis of FGMs, in: Functionally Graded Materials 1996. Elsevier, pp. 137–141. https://doi.org/10.1016/b978-044482548-3/50023-8

Quek, S.T., Wang, Q., 2000. On dispersion relations in piezoelectric coupled-plate structures. Smart Mater. Struct. 9, 859–867. https://doi.org/10.1088/0964-1726/9/6/317

Reddy, J.N., 2006. Theory and Analysis of Elastic Plates and Shells, Second Edition, Theory and Analysis of Elastic Plates and Shells, Second Edition. https://doi.org/10.1201/9780849384165

Rouleau, L., Deü, J.F., Legay, A., Le Lay, F., 2013. Application of Kramers-Kronig relations to time-temperature superposition for viscoelastic materials. Mech. Mater. 65, 66–75. https://doi.org/10.1016/j.mechmat.2013.06.001

Salehi, M., Aghaei, H., 2005. Dynamic relaxation large deflection analysis of non-axisymmetric circular viscoelastic plates. Comput. Struct. 83, 1878–1890. https://doi.org/10.1016/j.compstruc.2005.02.023

Salehi, M., Safi-djahanshahi, A., 2010. Non-Linear Analysis of Viscoelastic Rectangular Plates Subjected to In-Plane Compression. J. Mech. Res. Appl. 2, 11–21.

Saumya S., Naskar S., Mukhopadhyay T., 2023. 'Magic' of twisted multi-layered graphene and 2D nano-heterostructures, Nano Futures.
https://doi.org/10.1088/2399-1984/acf0a9

Shen, H.S., Xiang, Y., Lin, F., Hui, D., 2017. Buckling and postbuckling of functionally graded graphene-reinforced composite laminated plates in thermal environments. Compos. Part B Eng. 119, 67–78. https://doi.org/10.1016/j.compositesb.2017.03.020

Shingare, K.B., Naskar, S., 2023. Compound influence of surface and flexoelectric effects on static bending response of hybrid composite nanorod. J. Strain Anal. Eng. Des. 58, 73–90. https://doi.org/10.1177/03093247221096518

Singh, A., Naskar, S., Kumari, P., Mukhopadhyay, T., 2023. Viscoelastic free vibration analysis of in-plane functionally graded orthotropic plates integrated with piezoelectric sensors: Time-dependent 3D analytical solutions. Mech. Syst. Signal Process. 184, 109636. https://doi.org/10.1016/j.ymssp.2022.109636

Singh K., Shingare K. B., Mukhopadhyay T., Naskar S., 2023a. Multi-level fully-integrated electromechanical property modulation of functionally graded graphene-reinforced piezoelectric actuators: Coupled effect

of poling orientation, Advanced Theory and Simulations, 6(4) 2200756 https://doi.org/10.1002/adts.202200756

Sinha P., Mukhopadhyay T., 2023. Programmable multi-physical mechanics of mechanical metamaterials, Materials Science & Engineering R, 155, 100745. https://doi.org/10.1016/j.mser.2023.100745

Smith, W.A., Auld, B.A., 1991. Modeling 1–3 Composite Piezoelectrics: Thickness-Mode Oscillations. IEEE Trans. Ultrason. Ferroelectr. Freq. Control 38, 40–47. https://doi.org/10.1109/58.67833

Song, M., Kitipornchai, S., Yang, J., 2017a. Free and forced vibrations of functionally graded polymer composite plates reinforced with graphene nanoplatelets. Compos. Struct. 159, 579–588. https://doi.org/10.1016/j.compstruct.2016.09.070

Song, M., Yang, J., Kitipornchai, S., 2018. Bending and buckling analyses of functionally graded polymer composite plates reinforced with graphene nanoplatelets. Compos. Part B Eng. 134, 106–113. https://doi.org/10.1016/j.compositesb.2017.09.043

Song, M., Yang, J., Kitipornchai, S., Zhu, W., 2017b. Buckling and postbuckling of biaxially compressed functionally graded multilayer graphene nanoplatelet-reinforced polymer composite plates. Int. J. Mech. Sci. 131–132, 345–355. https://doi.org/10.1016/j.ijmecsci.2017.07.017

Stein, M., 1986. Nonlinear theory for plates and shells including the effects of transverse shearing. AIAA J. 24, 1537–1544. https://doi.org/10.2514/3.9477

Tanaka, K., Tanaka, Y., Enomoto, K., Poterasu, V.F., Sugano, Y., 1993. Design of thermoelastic materials using direct sensitivity and optimization methods. Reduction of thermal stresses in functionally gradient materials. Comput. Methods Appl. Mech. Eng. 106, 271–284. https://doi.org/10.1016/0045-7825(93)90193-2

Tita, V., De Medeiros, R., Marques, F.D., Moreno, M.E., 2015. Effective properties evaluation for smart composite materials with imperfect fiber-matrix adhesion. J. Compos. Mater. 49, 3683–3701. https://doi.org/10.1177/0021998314568328

Touratier, M., 1991. An efficient standard plate theory. Int. J. Eng. Sci. 29, 901–916. https://doi.org/10.1016/0020-7225(91)90165-Y

Trinh, M.C., Mukhopadhyay, T., Kim, S.E., 2020. A semi-analytical stochastic buckling quantification of porous functionally graded plates. Aerosp. Sci. Technol. 105. https://doi.org/10.1016/j.ast.2020.105928

Wang, Y., Xie, K., Fu, T., 2020. Vibration analysis of functionally graded graphene oxide-reinforced composite beams using a new Ritz-solution shape function. J. Brazilian Soc. Mech. Sci. Eng. 42. https://doi.org/10.1007/s40430-020-2258-x

Wenzel, M.J., Josse, F., Heinrich, S.M., 2009. Deflection of a viscoelastic cantilever under a uniform surface stress: Applications to static-mode microcantilever sensors undergoing adsorption. J. Appl. Phys. 105. https://doi.org/10.1063/1.3086626

Wu, H., Kitipornchai, S., Yang, J., 2017. Thermal buckling and postbuckling of functionally graded graphene nanocomposite plates. Mater. Des. 132, 430–441. https://doi.org/10.1016/j.matdes.2017.07.025

Yan, Z., Jiang, L., 2017. Modified continuum mechanics modeling on size-dependent properties of piezoelectric nanomaterials: A review. Nanomaterials. https://doi.org/10.3390/nano7020027

Yan, Z., Jiang, L., 2011. Surface effects on the electromechanical coupling and bending behaviours of

piezoelectric nanowires. J. Phys. D. Appl. Phys. 44. https://doi.org/10.1088/0022-3727/44/7/075404

Zenkour, A.M., 2007. Benchmark trigonometric and 3-D elasticity solutions for an exponentially graded thick rectangular plate. Arch. Appl. Mech. 77, 197–214. https://doi.org/10.1007/s00419-006-0084-y

Zenkour, A.M., Alghanmi, R.A., 2018. Bending of functionally graded plates via a refined quasi-3D shear and normal deformation theory. Curved Layer. Struct. 5, 190–200. https://doi.org/10.1515/cls-2018-0014

Zenkour, A.M., Hafed, Z.S., 2020. Bending analysis of functionally graded piezoelectric plates via quasi-3D trigonometric theory. Mech. Adv. Mater. Struct. 27, 1551–1562. https://doi.org/10.1080/15376494.2018.1516325

Zhao, Z., Ni, Y., Zhu, S., Tong, Z., Zhang, J., Zhou, Z., Lim, C.W., Xu, X., 2020. Thermo-Electro-Mechanical Size-Dependent Buckling Response for Functionally Graded Graphene Platelet Reinforced Piezoelectric Cylindrical Nanoshells. Int. J. Struct. Stab. Dyn. 20. https://doi.org/10.1142/S021945542050100X